

Retrieving 3D distributions of atmospheric particles using Atmospheric Tomography with 3D Radiative Transfer – Part 2: local optimization

Jesse Loveridge¹, Aviad Levis², Larry Di Girolamo¹, Vadim Holodovsky³, Linda Forster⁴, Anthony B. Davis⁴, Yoav Y. Schechner³

¹Department of Atmospheric Sciences, University of Illinois at Urbana-Champaign, Urbana, 61801, USA

²Computer and Mathematical Sciences Department, California Institute of Technology, Pasadena, 91125, USA

³Viterbi Faculty of Electrical and Computer Engineering, Technion – Israel Institute of Technology, Haifa 3200003, Israel

⁴Jet Propulsion Laboratory, California Institute of Technology, Pasadena, 91109, USA

10 *Correspondence to:* Jesse Loveridge (jesserl2@illinois.edu)

Abstract. Our global understanding of clouds and aerosols relies on the remote sensing of their optical, microphysical, and macrophysical properties using, in part, scattered solar radiation. Current retrievals assume clouds and aerosols form plane-parallel, homogeneous layers and utilize 1D radiative transfer (RT) models. These assumptions limit the detail that can be retrieved about the 3D variability of cloud and aerosol fields and induce biases in the retrieved properties for highly heterogeneous structures such as cumulus clouds and smoke plumes. In Part 1 of this two-part study, we validated a tomographic method that utilizes multi-angle passive imagery to retrieve 3D distributions of species using 3D RT to overcome these issues. That validation characterized the uncertainty in the approximate Jacobian used in the tomographic retrieval over a wide range of atmospheric and surface conditions for several horizontal boundary conditions. Here in Part 2, we test the algorithm’s effectiveness on synthetic data to test whether retrieval accuracy is limited by the use of the approximate Jacobian. We retrieve 3D distributions of volume extinction coefficient (σ_{3D}) at 40 m resolution from synthetic multi-angle, monospectral imagery at 35 m resolution derived from stochastically-generated ‘cumuliform’ clouds in $(1 \text{ km})^3$ domains. The retrievals are idealized in that we neglect forward modelling and instrumental errors with the exception of radiometric noise; thus reported retrieval errors are lower bounds. σ_{3D} is retrieved with, on average, a Relative Root Mean Square Error (RRMSE) $< 20\%$ and bias $< 0.1\%$ for clouds with Maximum Optical Depth (MOD) < 17 , and the RRMSE of the radiances is $< 0.5\%$, indicating very high accuracy in shallow cumulus conditions. As the MOD of the clouds increases to 80, the RRMSE and biases in σ_{3D} worsen to 60% and -35%, respectively, and the RRMSE of the radiances reaches 16%, indicating incomplete convergence. This is expected from the increasing ill-conditioning of the inverse problem with decreasing mean-free-path predicted by RT theory and discussed in detail in Part 1. We tested retrievals that use a forward model that is **better-conditioned less ill-conditioned (in terms of condition number)** but **also** less accurate due to more aggressive delta-M scaling. This reduces the radiance RRMSE to 9% and the bias in σ_{3D} to -8% in clouds with MOD ~ 80 , with no improvement in the RRMSE of σ_{3D} . This illustrates a significant sensitivity of the retrieval to the numerical configuration of the RT model which, at least in our circumstances, improves the retrieval accuracy. All of these ensemble-averaged results are robust to the inclusion of

radiometric noise during the retrieval. However, individual realizations can have large deviations of up to 18% in the mean extinction in clouds with MOD ~ 80 , which indicates large uncertainties in the retrievals in the optically thick limit. Using the
35 ~~better-conditioned~~ ~~less ill-conditioned~~ forward model tomography can also accurately infer optical depths (OD) in conditions spanning the majority of oceanic, cumulus fields (MOD < 80) as the retrieval provides OD with bias and RRMSE better than -8% and 36%, respectively. This is a significant improvement over retrievals using 1D RT, which have OD biases between -30% and -23% and RRMSE between 29% and 80% for the clouds used here. Prior information or other sources of information will be required to improve the RRMSE of σ_{3D} in the optically thick limit, where the RRMSE is shown to have strong spatial
40 structure that varies with the solar and viewing geometry.

1 Introduction

Remote sensing retrievals of cloud and aerosol properties are important contributors to our understanding of cloud and aerosol processes and constraining the emergent behaviour of these processes on Earth's climate (Bellouin et al., 2020; Sherwood et al., 2020). As atmospheric modelling has become more complex, there has been an increased demand for high quality
45 observations to constrain the uncertain processes within the models and inform model development (Morrison et al., 2020). New observational techniques are required that can provide robust statistics of small-scale, spatially resolved, cloud and aerosol microphysical parameters, so that their controlling processes can be constrained in both high- and low-resolution modelling.

In Part 1 of this study (Loveridge et al., 2023), we described a remote sensing retrieval technique with the potential to meet
50 these needs by providing 3D instantaneous snapshots of volumetric properties of the atmosphere at the resolution of passive imagery. Our method uses multi-angle imagery and the Spherical Harmonics Discrete Ordinates Method (SHDOM) (Evans, 1998) for modelling 3D Radiative Transfer (RT) to constrain the 3D properties of atmospheric particles, such as effective particle radius and mass concentration (Levis et al., 2020; Tzabari et al., 2022), in a process called tomography (Arridge and Schotland, 2009; Martin et al., 2014). Our retrieval algorithm for the tomography problem directly builds upon earlier work in
55 making such retrievals tangible and computationally efficient through the use of approximate Jacobians of 3D radiative transfer that enable the use of efficient gradient-based local optimization methods (Levis et al., 2015, 2017, 2020). We have made our method publicly available in the software package Atmospheric Tomography with 3D Radiative Transfer (AT3D) (Loveridge et al., 2022a), which was developed from the research software used in Levis et al. (2015, 2017, 2020) called pySHDOM.

60 Our tomographic algorithm retrieves 3D properties and makes use of 3D RT. In doing so it relaxes the twin assumptions of independent pixels and homogeneous plane-parallel clouds that cause significant biases in operational retrievals of cloud microphysical properties (Marshak et al., 2006; Kato and Marshak, 2009; Zhang et al., 2012; Lebsock and Su, 2014; Ahn et al., 2018; Fu et al., 2019; Painemal et al., 2021; Fu et al., 2022). Another key advantage of the method is that it does not rely on expensive active remote sensing for retrieving volumetric information as in other methods (Fielding et al., 2014). Instead,

65 the method only relies on relatively inexpensive passive imaging in the solar part of the spectrum. It thereby enables wide
swath widths and high-resolution retrievals with high Signal-to-Noise Ratio and high sensitivity to scattering particles in the
size range of atmospheric clouds and aerosols (Dubovik et al., 2011; King and Vaughan, 2012; Ewald et al., 2021). These
benefits position the tomographic retrieval as a means of filling the observational gap that exists for the highly heterogeneous
fields of cumulus that are climatically important (Sherwood et al., 2014).

70

It is still unclear exactly how effective tomography will be across the range of scattering regimes present in the Earth's
atmosphere. The development of tomographic retrievals in atmospheric science is at an early stage where numerical tests have
yet to consider the full complexity of Earth's atmosphere and surface (Martin and Hasekamp, 2018; Levis et al., 2020; Doicu
et al., 2022b; Tzabari et al., 2022). This two-part study contributes to further our understanding of the effectiveness of cloud
75 tomography. In Part 1 of our study, we evaluated the accuracy of our approximate Jacobian for the first time and established
the theory behind its effectiveness. We identified a number of issues that may occur when applying the approximate Jacobian
to solve a cloud tomography problem using local optimization, particularly due to the non-linearity of the problem and the loss
of sensitivity of the measurements in the diffuse-scattering limit (Levis et al., 2015; Martin and Hasekamp, 2018; Forster et
al., 2021; Davis et al., 2021). Our goal here in Part 2 is to test the efficacy of our proposed retrieval algorithm for retrieving
80 3D volume extinction coefficient across a wide range of scattering regimes, though still in idealized conditions. For the first
time, we compare cloud optical depths inferred from the tomographic retrieval against those retrieved using a 1D radiative
transfer model. In Section 2, we formulate the tomography problem and review relevant past work on inverse radiative transfer,
summarizing key discussions and results from Part 1 where appropriate. Section 3 presents our idealized methodology to test
the efficacy of the retrieval numerically. We test our retrieval on synthetic radiances calculated from stochastically generated
85 clouds and examine the influence of the cloud optical depth on the retrieval accuracy. We also explore the influence of using
an approximate forward model and introducing radiometric noise on the retrieval accuracy. Our results are presented in Section
4 and we discuss their implications in Section 5 and highlight important areas of future work in the development of tomographic
retrievals. We present our conclusions in Section 6.

2. Background

90 The objective of the tomographic retrieval, as formulated in AT3D, is to select a state vector (\mathbf{a}) that parameterizes a discrete
representation of the atmospheric optical or physical properties and best fits the available measurements (\mathbf{y}) and any prior
knowledge of the unknown state. The selection of the best fitting state vector is done by minimizing the scalar cost function
which penalizes misfit against observations in a generalized, least-squares sense:

$$\chi^2 = (\mathbf{y} - \mathbf{F}(\mathbf{a}))^T \mathbf{S}_\epsilon^{-1} (\mathbf{y} - \mathbf{F}(\mathbf{a})) + R(\mathbf{a}). \quad (1)$$

95 In this expression, \mathbf{S}_ϵ , is the error covariance matrix of the residual between the measurements (\mathbf{y}) and the forward model $\mathbf{F}(\mathbf{a})$ and accounts for both measurement uncertainty and forward model uncertainty. $R(\mathbf{a})$ is a differentiable regularization term that reflects prior knowledge about the unknown state vector. The forward model $\mathbf{F}(\mathbf{a})$ consists of a solution of the 3D RTE and a sampling operation that provides the forward-modelled Stokes vector at the positions and angles sampled by a sensor during the acquisition of the measurements, \mathbf{y} .

100

The solution to the inverse problem can be stated formally as the selection of the state vector $\tilde{\mathbf{a}}$, that minimizes the cost function subject to box constraints. The box constraints are vectors of lower bounds (\mathbf{l}) and upper bounds (\mathbf{u}) on each element of the state vector to ensure a valid range for physical variables. For example, liquid water content or volume extinction coefficient should be non-negative. We then have:

$$105 \quad \tilde{\mathbf{a}} = \underset{\mathbf{a}}{\operatorname{argmin}} \chi^2, \quad \text{s.t.} \quad \mathbf{l} \leq \mathbf{a} \leq \mathbf{u}. \quad (2)$$

A local minimization method such as the Limited memory-Broyden-Fletcher-Goldfarb-Shannon method for Bounded minimization (L-BFGS-B) (Byrd et al., 1995) solves Eq. 2 for a locally optimal state vector. Figure 1 presents a flowchart of this process. To use such a method, we need to be able to compute the gradient of the cost function. The gradient of the data-fit component of the cost function is given by:

$$110 \quad \frac{\partial \chi^2}{\partial \mathbf{a}} = 2(\mathbf{y} - \mathbf{F}(\mathbf{a}))^T \mathbf{S}_\epsilon^{-1} \mathbf{K} + \frac{\partial R(\mathbf{a})}{\partial \mathbf{a}}, \quad (3)$$

where \mathbf{K} is the Jacobian matrix containing the partial derivatives of the i^{th} output of the forward model with respect to the j^{th} component of the state vector:

$$K_{ij} = \frac{\partial F_i(\mathbf{a})}{\partial a_j}. \quad (4)$$

We use the approximate Jacobian matrix calculation described in Part 1 (Loveridge et al., 2023) to efficiently compute
115 approximate gradients of the cost function using the approximate Jacobian $\tilde{\mathbf{K}}$:

$$\frac{\partial \chi^2}{\partial \mathbf{a}} \approx 2(\mathbf{y} - \mathbf{F}(\mathbf{a}))^T \mathbf{S}_\epsilon^{-1} \tilde{\mathbf{K}}. \quad (5)$$

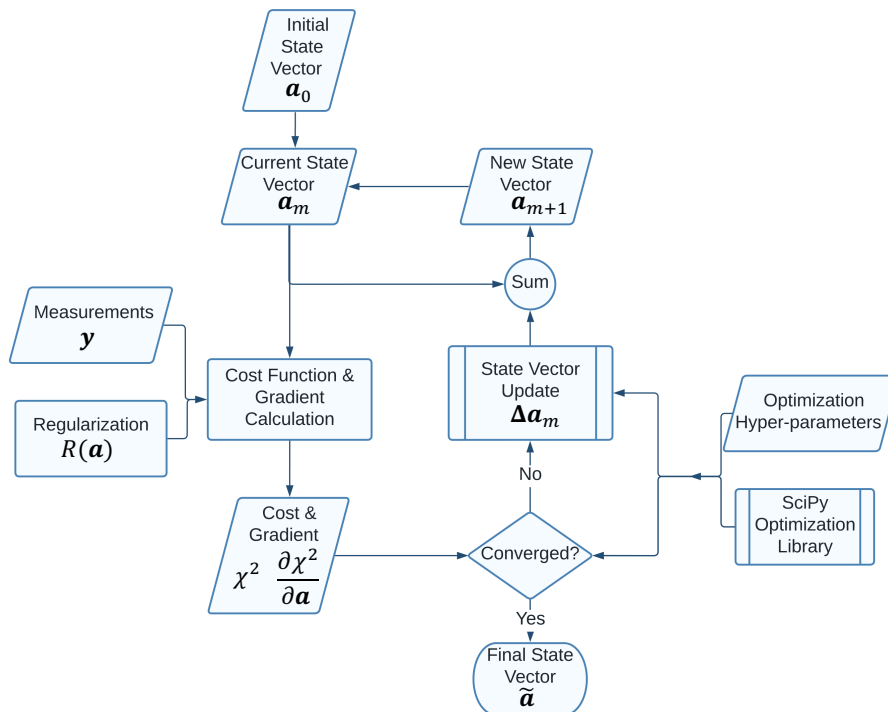


Figure 1: A flowchart depicting the overall iterative retrieval methodology of AT3D reproduced from Part 1 (Loveridge et al. 2022). Sections 3.2 and 3.2.1 describe some of the details of how the initial state vector and optimization hyper-parameters are chosen, along with a procedure for synthetically generating some measurements using AT3D.

Our approximate Jacobian matrix is accurate in the single-scattering limit. In this regime, it has a relative Root Mean Square Error (RMSE) of 4% with respect to finite differencing calculations (Loveridge et al., 2023), similar to the accuracy of derivatives calculated using a forward-adjoint formulation (Doicu and Efremenko, 2019). The accuracy of the approximate Jacobian degrades as the medium becomes optically thicker, the phase function becomes more isotropic, and as the single-scatter albedo and surface albedo increase (Loveridge et al., 2023). This is due to the larger relative contributions of higher-order scattering to the gradients, which are the contributions which are least accurately modelled in our approximate Jacobian calculation (Loveridge et al., 2023). When the medium has single-scattering properties representative of cloud droplets at visible wavelengths and the surface is dark (e.g., oceanic) then the relative RMSE in the approximate Jacobian reaches only 12% for finite clouds with maximum optical depths of 100 (Loveridge et al., 2023).

The accuracy of the approximate Jacobian also varies with the angular resolution of the SHDOM solver when phase functions have strong forward scattering peaks (Loveridge et al., 2023). This occurs due to the interaction of the angular resolution and the delta-M scaling (Wiscombe, 1977) and Truncated Multiple Scattering (TMS) approximations (Nakajima and Tanaka, 1988) used in SHDOM. Lower angular resolution results in more scattering being treated as part of the direct transmission. This results in a decrease in the effective optical thickness of the medium and a corresponding increase in the accuracy of the

approximate Jacobian. If the angular resolution is lowered from 16 zenith angle discrete ordinate bins to just two zenith angle discrete ordinate bins then the error in the approximate Jacobian decreases from 12% to 8% for the cloud like media described above.

140 Errors in the Jacobian calculation lead to errors in the gradient which limit the convergence of a local optimization method such as the L-BFGS-B method. This is because, in the presence of errors, only small step sizes will accurately predict the change in the cost function to a precision that satisfies the stability criteria in the line search of the optimization procedure (Byrd et al., 1995; Zhu et al., 1997). If errors in the gradient are large, then the optimization may terminate far from an apparent minimum in the cost function even when the optimization problem is linear (Shi et al., 2021).

145

There are several factors that complicate this retrieval methodology which uses local optimization. These factors have been discussed in Part 1 and elsewhere in the literature. In the remainder of this section, we briefly summarize these factors which motivate our study and its methodology. In addition to the uncertainties due to our approximate Jacobian calculation, the use of a local optimization method on a non-linear inverse problem also introduces significant uncertainty. As the forward model
150 $\mathbf{F}(\mathbf{a})$ is non-linear, multiple local minima in the cost function may exist. This means that the best-fitting state vector estimated from local optimization methods may be strongly sensitive to the choice of initialization and may be far from the globally optimal solution (Rodgers, 2000). Linearized uncertainty estimates may also be inaccurate (Rodgers, 2000; Gao et al., 2022). So far, only local optimization methods have been employed for physics-based cloud tomography (Martin and Hasekamp, 2018; Levis et al., 2020; Doicu et al., 2022b). The proposed BFGS algorithm performs well compared to other local
155 optimization techniques (Doicu et al., 2022a). Global optimization methods such as ensemble-based particle filters (van Leeuwen et al., 2019) have also been proposed for tomography in other fields (Raveendran et al., 2011). Interestingly, it has been shown that our approximate Jacobian can outperform an “exact” linearization using forward-adjoint methods which was suggested to be due to the ability of the approximate Jacobian to escape local minima (Doicu et al., 2022b).

160 The use of a local optimization method introduces the need to choose a particular initialization for each retrieval. This choice is non-trivial, especially as clouds become optically thick. A poor choice for the spatial distribution of the extinction coefficient, even with a correct average mean-free-path (or optical diameter), may degrade the retrieval performance. This is because the distribution of an optically thick medium in space is highly non-linear, while adjusting the extinction coefficient within a known volume is weakly non-linear. It has been shown that when the ground truth cloud envelope is used to initialize the
165 retrieval, then the performance of the retrieval improves substantially (Tzabari et al., 2022).

In addition to the complexity of selecting an initial guess appropriate for an optically thick cloud, local optimization is expected to become much more difficult in the regions of state space where clouds are optically thick. This is due to the ill-conditioning of the forward model (Liveridge et al., 2023). The degree of ill-conditioning of an operator measures its instability to inversion.

170 The condition number of the Jacobian matrix, $\kappa(\mathbf{K})$, is the upper bound for the relative enhancement of an error in the measurement space when it is propagated by the Jacobian matrix to the state space. We measure the magnitude of errors in a vector using the commonly used 2-norm, so then the condition number of a matrix is defined as the ratio of its largest (s_1) and smallest (s_n) singular values:

$$\kappa(\mathbf{K}) = \frac{s_1}{s_n}. \quad (6)$$

175 In Part 1, we showed that the condition number increases exponentially from well-conditioned $\kappa(\mathbf{K}) \sim 10^1$ to very ill-conditioned $\kappa(\mathbf{K}) \gg 10^5$ as the optical depth of the medium increases from 0.1 to 100.0 for finite clouds (Loveridge et al., 2023). **The largest condition numbers in clouds with maximum optical depths of 100 were associated maximum and minimum singular values of 0.06 and 2e-7. The absolute magnitude of these singular values is associated with uncertainty propagation via the Fisher information matrix, but are also sensitive to the details of the discretization such as grid spacing.** A condition
180 number that is comparable to or larger than the inverse of the numerical precision of any floating-point numbers is effectively ill-posed as even rounding errors can propagate to large uncertainties. The exponential behaviour of the condition number is in agreement with theoretical estimates of the stability of the continuous RT problem (Bal and Jollivet, 2008; Chen et al., 2018; Zhao and Zhong, 2019), perturbative numerical studies of radiative transfer in cloudy atmospheres (Martin and Hasekamp, 2018; Forster et al., 2021), and the field of Diffuse Optical Tomography (DOT) (Tian et al., 2010; Niu et al., 2010; Raveendran
185 et al., 2011). This behaviour is due to the smoothing effect of multiple scattering. A smoothing operator is unstable under inversion. This effect of radiative smoothing has been the subject of study in cloudy atmospheres (Marshak et al., 1995; Davis et al., 1997) in the context of optical depth retrieval, but is enhanced in a tomographic context due to the finer 3D discretization of the medium (Bal, 2012).

190 The ill-conditioning in optically thick clouds results in uncertainties that are not evenly distributed throughout the cloud. It has been shown that measurements first lose sensitivity to changes in the cloud in the regions that are optically far from all sensors and also the sun (Niu et al., 2010; Tian et al., 2010; Forster et al., 2021; Loveridge et al., 2023). This will result in the largest uncertainties in those regions. In Part 1, we also hypothesized that the large mismatch in sensitivities between these regions and the outer edges and illuminated sides of the optically thick clouds would cause systematic errors in retrievals that use local
195 optimization. There is some indication that this effect occurs in practice as retrievals performed with an optically thin initialization have underestimations of extinction in the centre of clouds, especially when they are thicker (Levis et al., 2015; Martin and Hasekamp, 2018). One focus of our work is to quantify the extent to which such systematic errors emerge in our retrievals.

200 In Part 1, we also identified that the magnitude of the loss of sensitivity and ill-conditioning of the forward model in the optically thick limit can be dramatically reduced by lowering the angular resolution of the SHDOM model (Loveridge et al., 2023). This is again due to the interaction of the delta-M scaling with the angular resolution of the model due to the lowering

of the effective optical depth of the radiative transfer. For the same finite clouds described above, the decrease in the magnitude of the condition number of the Jacobian matrix can reach a factor of $\sim 10^2$ when lowering the angular resolution from 16 zenith angle discrete ordinate bins to just 2 zenith angle discrete ordinate bins. This means that a lower accuracy SHDOM model is less ill-conditioned (due to its lower condition number). The reduction in condition number is due to more sensitivity to the interior of an optically thick cloud and may be useful for improving retrieval accuracy despite its larger forward modelling error. This property is independent of our approximation to the Jacobian matrix (Loveridge et al., 2023). The reduction in condition number of the forward model with decreasing angular resolution, the increase in the accuracy of the approximate Jacobian with decreasing angular resolution stem from the same cause but have different effects on a local optimization procedure. Ill-conditioning is the sensitivity of the inversion to errors. The approximation to the Jacobian is a source of error.

The objective of our study is to examine the effectiveness of the local optimization method described in Part 1 to perform cloud tomography. As part of this, we also test the sensitivity of the local optimization to the optical depth of the cloud and to the angular accuracy used in the forward model, SHDOM. Low accuracy forward models are frequently used to accelerate the iterative solution of optimization problems (Tarvainen et al., 2009; Peherstorfer et al., 2018) and our analysis below provides a first test of whether this approach may also be beneficial in the context of cloud tomography to reduce computational cost.

3 Methods

We perform retrievals on synthetic clouds with stochastically generated 3D fields of volume extinction coefficient. These synthetic clouds are designed to resemble cumuliform clouds and have maximum optical depths that range from 4 to 88. The technical details of the procedure for generating these synthetic measurements for a range of clouds across a range of optical depths is described in Section 3.1. We perform retrievals of the 3D volume extinction coefficient using perfect knowledge of the ground-truth atmosphere, surface, and cloud microphysics. This idealized configuration is sufficient to test the efficacy of the approximate Jacobian. We initialize our local optimization by assuming that the cloud is extremely optically thin, which has been exclusively used so far in cloud tomography (Levis et al., 2015, 2017; Martin and Hasekamp, 2018; Levis et al., 2020; Doicu et al., 2022a, b). The precise methodology we use is described in Section 3.2 and the associated appendices. This configuration acts as a limiting case as the local optimization will be tested by the high degree of non-linearity of the forward model between its optically thin initialization and the, potentially optically thick, ground truth. As such, we must stress that our results are likely particular to this choice.

To isolate the fundamental limitations in using the local optimization method with the approximate Jacobian, we perform our analysis in an idealized numerical setting. We perform several “inverse crimes” in our retrievals by choosing the discretization of the retrieved medium to perfectly match the ground truth and neglecting several important sources of uncertainty such as forward model error and instrument calibration uncertainties. The first of these approximations has been routine throughout

235 numerical studies of cloud tomography (Levis et al., 2015, 2017; Martin and Hasekamp, 2018; Levis et al., 2020; Doicu et al.,
2022a, b; Tzabari et al., 2022). Such approximations are also common in the assessment of other algorithms for atmospheric
remote sensing, where synthetic measurement data are often generated using the same 1D radiative transfer model used to
perform the retrievals (Delanoë and Hogan, 2008; Xu et al., 2022). Such simplifications occur despite the fact that this
approximation is known to fundamentally simplify the nature of the inverse problem and thereby cause underestimates of the
240 true retrieval error (Rodgers, 2000; Bal, 2012). Within radiative transfer, a fixed discretization error also implies a homogeneity
assumption below a scale that is likely unrealistic for real clouds, which can cause biases in the resulting modelling of the
radiative transfer (Marshak et al., 1998; Davis and Marshak, 2004; Bitterli et al., 2018).

Measurement noise tends to decrease from 1% to just 0.1% for cloudy signals as the measured radiance increases (Bruegge et
245 al., 2002). Measurement noise has typically been included in cloud tomography studies so far (Levis et al., 2015, 2020; Tzabari
et al., 2022) although in some cases, this source of uncertainty has also been neglected (Doicu et al., 2022a, b). The magnitude
of this noise is much smaller than forward modelling errors that can range up to several percent in a root-mean-square sense
(Evans, 1998; Cahalan et al., 2005; Pincus and Evans, 2009). These uncertainties have been neglected so far with the exception
of the study of Martin et al. (2018), which used an inflated measurement error of 2% as a proxy for the modelling error.

250

In our study, we perform sets of retrievals that use both perfect, noise-free measurements and also those that include idealized
measurement noise to ensure that our conclusions about the fidelity of the retrieval are robust to the noise free assumption.
Even with this analysis, we must emphasise that our retrievals are highly simplified and so the errors in our retrievals should
only be interpreted as a tentative lower bound for errors that might occur for retrievals applied to real data.

255

We analyse seven types of retrieval. Firstly, we have perfect model retrievals, in which we use the exact same forward model
configuration and discretization of the medium during the retrieval that was used to generate the synthetic measurements. This
type of retrieval uses noise free measurements and the naïve, optically thin initialization which we describe in Section 3.2.
These retrievals are referred to as “Default” retrievals. Retrieval accuracy in this configuration is limited only by the non-
260 linearity of the inverse problem and the errors in the approximate Jacobian, both of which are deterministic.

Secondly, we perform retrievals that are the same as the “Default” except they use a low angular accuracy forward model.
These are referred to as “Low” retrievals. This retrieval acts as a test of how much the retrieval changes when using an
approximate forward model that is **less ill-conditioned (has a lower condition number)** and has a more accurate gradient
265 calculation. The differences between the “Default” and “Low” retrievals may occur as a result of changes in the optimization
trajectory either close-to or far from the local minimum in the cost function. To distinguish between these two types of effects,
we perform a third set of retrievals. These retrievals use the same configuration as the “Low” retrieval except they are initialized
at the ground truth and are referred to as “Low-GT”. The drift in the state vector away from the ground truth during the

270 optimization acts as a measure of the error induced by using a low angular accuracy model in the retrieval in the vicinity of the global minimum.

We also include two sets of restarted retrievals. The restarted retrievals make use of the results of the “Low” retrievals to initialize retrievals that use the perfect forward model from the “Default” retrievals. These restarted retrievals are referred to as “20th Low iteration Restart” and “Final Low iteration Restart” based on the iteration of the “Low” retrievals from which the state vector is taken to initialize the new restarted retrieval. These retrievals test our ability to mitigate any errors forming in the Low retrievals by using the perfect forward model.

280 Additionally, we perform two sets of experiments to ensure the robustness of our conclusions to the presence of noise or other small inconsistencies between the synthetic measurements and the forward model. Firstly, we perform retrievals initialized at the ground truth that make use of noisy measurements and the perfect model from the “Default” retrievals. These are referred to as “Noisy-GroundTruth” retrievals. Secondly, we repeat the “Default” and “Low” experiments using noisy observations and use the differences to assess the robustness of our results. These retrievals are referred to as “Default-Noisy” and “Low-Noisy”.

3.1 Synthetic Measurement Generation

285 We generate the synthetic measurements entirely using cloud fields, RT, and instrument modelling implemented in AT3D. The only scattering particle species under consideration in each retrieval is an isolated water cloud (i.e., no molecular scattering or absorption). We assume that the cloud scattering is conservative ($\omega = 1$) and the phase function is from Mie calculations of a gamma distribution of spherical water droplets with an effective radius of 10 microns and effective variance of 0.1 at a wavelength of 0.86 microns. Vacuum horizontal boundary conditions are used and the bottom surface is prescribed to be black.

290 There is only a solar source, no thermal emission.

The clouds used in this study are stochastically generated rather than generated by Large Eddy Simulations, as is common in many retrieval validation studies (Marshak et al., 2006; Kato and Marshak, 2009; Ewald et al., 2019). This choice is made primarily for control over the media. Realistic covariances between microphysical parameters, which is one of the primary benefits of LES (Miller et al., 2018), are not required for these retrievals as only a single spatially variable parameter is being retrieved (i.e., volume extinction coefficient). With stochastic generation we can control the spatial variability at all scales and produce “difficult”, non-smooth extinction fields at scales of tens of meters with great ease that would otherwise require undue computational expense with LES.

300 The stochastic cloud generator used to generate the extinction fields is included with AT3D. It is based on similar statistical principles utilized elsewhere for synthetic cloud generation (Cahalan et al., 1994; Iwabuchi and Hayasaka, 2002; Prigarin and

Marshak, 2009). Such principles include the fact that liquid water content tends to have a positively skewed distribution (e.g. lognormal) and the power spectrum of its variability tends to follow a power law (Davis et al., 1999). The unique aspect of this generator is that it is targeted at generating isolated clouds rather than large fields with periodic boundaries. The algorithm proceeds as follows:

1. Two fields of white, gaussian noise with zero mean and unit variance are generated with skewness < 0.1 and kurtosis < 0.5 . One will form the binary volumetric cloud mask and the other will form the 3D field (e.g. extinction or liquid water content). This separation is done so that the smoothness of the cloud boundary can be controlled independently. It also introduces additional small-scale variability to the field by allowing large discontinuities between in-cloud and cloud-free field values.
2. The fast Fourier transform (FFT) of each field is obtained and then scaled so that the power spectrum follows a power law with a specified exponent. We used an exponent of $-5/3$ which is supported by various in situ measurements of horizontal variability of cloud liquid water content (Davis et al., 1996, 1999) as well as nadir radiance measurements (Lovejoy et al., 1993; Lewis et al., 2004). The resulting fields are then inverse Fourier transformed back into physical space.
3. The two fields are exponentiated to obtain positively skewed (e.g. lognormal) statistics typical of clouds.
4. The cloud mask field X is scaled by an anisotropic Butterworth filter in physical space to enforce small values near the boundaries of the domain. This counteracts the periodic nature of the FFT process used to generate the noise and allows generation of isolated clouds that have a “blob” shape that tends to maximize in the centre of the domain. Note there is no specific requirement for a single contiguous cloud mass, though this filter does encourage it. The filtered cloud mask field \tilde{X} is expressed as

$$\tilde{X} = \frac{X}{\sqrt{1 + \left(\frac{R}{\alpha}\right)^8} \sqrt{1 + \left(\frac{z'}{\beta}\right)^8}} \quad (7)$$

where R is the horizontal distance from the centre of the domain and z' is the vertical distance from the centre of the domain. The two scale parameters are set to $\alpha = 0.2$ and $\beta = 0.2$.

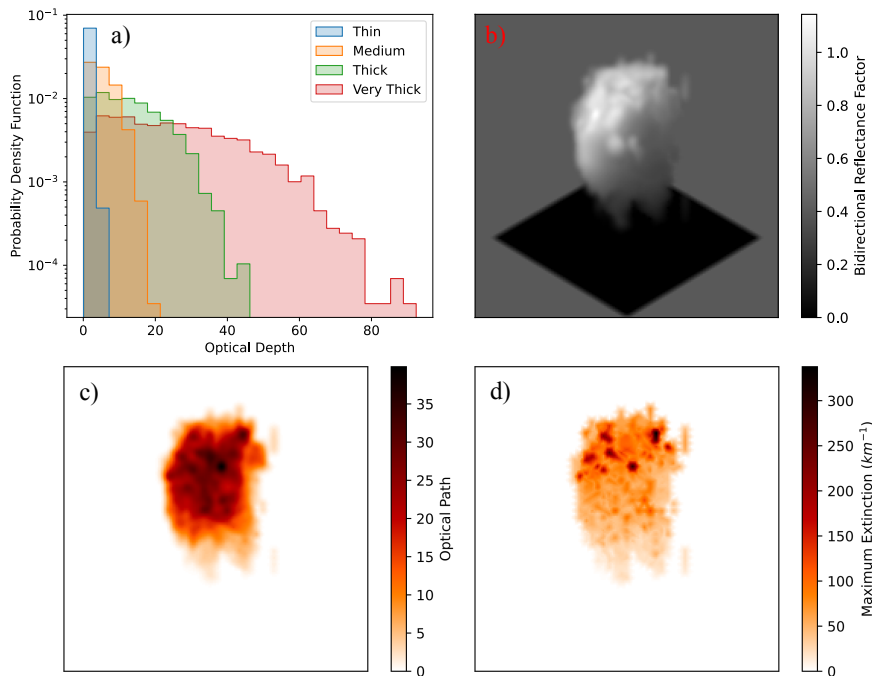
5. The cloud mask field is then thresholded to obtain a user specified volume cloud fraction of 10%.
6. The points in the second field are set to zero where the cloud mask field is designated as clear.
7. The second field is scaled so that its mean and variance have a user-specified vertical profile over the cloudy points and forms the 3D field of, for example, volume extinction coefficient.

We use 10 different random seeds and four different vertical profiles of horizontally-averaged extinction, thus generating 40 cloud models in four categories of maximum optical depth. Each of the four profiles prescribes a linear increase of mean extinction with height. Note that this is a more rapid increase of extinction with height than predicted by adiabatic theory,

namely, extinction increases as $\sigma(h) \sim h^{2/3}$, with h being the height above cloud base. At each level, the deviations from the mean are scaled so that the standard deviation is chosen to be 40% of the mean at that level. Each cloud is generated on a grid of (25 x 25 x 25) grid-points with 40 m resolution forming a domain of (1 km)³. We name the four categories of cloud models, Thin, Medium, Thick, and Very Thick. They have maximum vertical optical depths of 4, 17.5, 44, and 88, respectively.

Figure 2a shows the optical depth distributions of each of the four categories of clouds (left panel). For one example cloud realization, we also show an image of the cloud (Fig 2b) as well as the optical path and maximum volume extinction coefficient along the same lines of sight. These figures show the high degree of variability in the extinction fields (Fig. 2d) and the decorrelation of the optical path from the radiance field (Fig. 2b vs Fig 2c) due to the non-local transport process. Note that the decoupling of the extinction and cloud mask fields in the stochastic generator can produce true voids within the cloud. The cross sections of the extinction field (e.g., Figure 4) of a cloud reveals that the extinction fields can be much more variable than might be expected from an LES generated cloud at small scales (Eytan et al., 2022). This is a carefully considered choice as we want to test the limits of the retrieval on non-smooth media to detect, for example, a smoothing bias.

Figure 2: (a) The probability density functions of cloud optical depth for stochastically generated clouds in the Thin, Medium, Thick and Very Thick categories. Each category contains 10 clouds. (b) A volume rendering of the 3D volume extinction coefficient of the 1st cloud realization from the Very Thick category of stochastically generated clouds. The volume rendering was created using the Plotly software.



355 **Figure 3: (a) The probability density functions of cloud optical depth for stochastically generated clouds in the Thin, Medium, Thick and Very Thick categories. Each category contains 10 clouds. (b) An image of cloud realization #4 in the Thick category calculated using SHDOM. The setup is identical to the other simulations ($SZA = 60^\circ$) apart from the fact that the $(1 \text{ km})^3$ domain is surrounded by a Lambertian surface with an albedo of 0.4 to give a sense of perspective, which does affect the radiance calculation. The image is captured using a synthetic sensor following a perspective projection that has a 2.5° field of view with 200 by 200 pixels and is viewing the centre of the domain from a position of $x = y = z = 20 \text{ km}$ (central viewing zenith angle of 55° and relative azimuthal angle of 45°). (c) The optical path along each pixel's line of sight under the same projection as b). The maximum value of the volume extinction coefficient along the line of sight under the same projection as b). Two cross-sections through this cloud are also shown in Figure 6.**

The synthetic measurements used in this study are chosen to mimic an airborne multi-angle imager such as AirMSPI operating in step-and-stare mode (Diner et al., 2013), with the exception that all measurements are acquired simultaneously in this synthetic scenario. This is a similar configuration to that which can be achieved with the upcoming Cloud-CT mission (Schilling et al., 2019), which will utilize a constellation of small satellites to obtain simultaneous multi-angle imagery. Here, we model the imaging geometry as orthographic projections of the domain with a fixed azimuthal orientation at right angles with the principal plane of the Sun, i.e., relative azimuth of 90° and -90° . The use of an orthographic projection is a highly approximate camera model, but is suitable for approximating a small domain near the centre of the swath of a push-broom sensor. In addition to a nadir view there are images with viewing zenith angles of $[75.0^\circ, 60.0^\circ, 45.6^\circ, 26.1^\circ]$ on either side of the principal plane for a total of 9 views. This is the most used viewing angle configuration that has been used to test a 3D tomographic retrieval and has demonstrated success in several cases (Levis et al., 2015, 2017, 2020; Doicu et al., 2022a, b); so it forms a useful reference configuration on which to test the variation of retrieval accuracy with optical depth to help connect with other published results.

375 The solar zenith angle is chosen as 60° . This differs from other studies which have typically used a smaller solar zenith angle (Levis et al., 2015, 2017, 2020; Doicu et al., 2022a, b). We chose the larger value so that we can more easily discern the effects of any error features that are oriented with respect to the sun in our results as was hypothesised in Part 1. This choice also puts the observations close to the scattering angles of maximum error in the approximate Jacobian (see Part 1, where we quantified the scattering angle dependence of the error in the approximate Jacobian calculation); hence a worst-case scenario.

380 The measurement resolution is set to 35 m. AT3D models pixel-level radiance measurements as a weighted sum of idealized singular samplings of the radiance field within a field-of-view. For simplicity we choose a single quadrature point at each pixel center to model the pixel radiance in the simulation of the synthetic measurements. Choosing the measurement resolution (35 m) to be slightly smaller than the grid resolution (40 m) ensures that all of the grid points are evenly sampled by the measurements even with the single quadrature point per pixel. This ensures the basic numerical stability of the retrieval, by ensuring it is over constrained and that the use of regularization is not a strict requirement. The SHDOM solver uses 16 zenith discrete ordinate bins, 32 azimuthal discrete ordinate bins, a splitting accuracy of 0.03 and a solution accuracy of 10^{-4} with no truncation of the spherical harmonics. The scalar approximation (no polarization) to the RTE is utilized.

390 In the Default-Noisy, Low-Noisy and Noisy-GroundTruth experiments, noise is included in the measurements. The noise model used for this procedure is described in Appendix A. For each of the 40 sets of measurements, a fixed set of noise perturbations are generated through the selection of a random seed. These same noisy measurements are utilized in all retrieval experiments that make use of noisy measurements.

3.2 Inverse Problem Setup

395 The same forward model described above is used in most of the experiments except our Low retrievals. In these retrievals the angular accuracy in the SHDOM solver is reduced to just two zenith discrete ordinate bins and 4 azimuthal discrete ordinate bins. All other numerical parameters are the same.

The state vector is chosen as a subset of the grid points that are potentially cloud containing according to a space carving procedure (Kutulakos and Seitz, 1999) that uses 2D binary cloud masks from each of the multi-angle images (Lee et al., 2018). This procedure follows Levis et al. (2020). The space carving procedure rules out cloud along the line of sight of all pixels that are classified as clear. The details of the space carving algorithm and its performance are presented in Appendix B. The cloud masking of the multi-angle images is trivial due to the absence of a scattering surface or atmosphere (Yang and Di Girolamo, 2008). For the retrievals that use a naïve, optically thin initialization, the elements of the state vector are set as 0.01 km^{-1} .
 405 Additional description of the hyper-parameters of the optimization using the L-BFGS-B algorithm including the stopping conditions are in Appendix C.

4 Results

We now present the results of the retrievals and discuss the accuracy of the retrieved extinction fields and their robustness to noise (Section 4.1), the accuracy of inferred optical depths (Section 4.2), and the computational expense (Section 4.3). To
 410 quantify the performance of the extinction retrieval we use the relative bias and relative RMSE of the volume extinction field, expressed respectively as:

$$\text{Relative Bias} = 100\% \times \frac{\|\sigma_{\text{retrieved}}\|_1 - \|\sigma_{\text{truth}}\|_1}{\|\sigma_{\text{truth}}\|_1}, \quad (6)$$

$$\text{Relative RMSE} = 100\% \times \frac{\|\sigma_{\text{retrieved}} - \sigma_{\text{truth}}\|_2}{\|\sigma_{\text{truth}}\|_2}, \quad (7)$$

where $\|\mathbf{x}\|_1 = \sum_i |x_i|$ and $\|\mathbf{x}\|_2 = (\sum_i x_i^2)^{1/2}$.

415 where σ is the volume extinction coefficient. We also calculate the relative bias in the coefficient of variation (Standard Deviation divided by Mean) of the retrieved extinction field to quantify the heterogeneity of the retrieved cloud. We also apply these three metrics to the assessment of other variables such as optical depth. We refer to the error metrics in units of percent

(%) within the text for clarity. Simple differences in the error metrics between two retrievals are also reported in percent. Error metrics are defined by comparison with respect to the ground truth unless otherwise specified.

420

The error metrics are evaluated over all grid points in the $(1 \text{ km})^3$ domain, not the elements of the state vector, which only includes the grid points specified as cloudy by the space carving algorithm. In general, the fidelity of a 3D retrieval should be evaluated over the physical fields in the domain rather than a metric on the state vector space. This facilitates comparison with other retrieval methods which may not use the same spatial basis. The relative Bias and relative RMSE of the extinction field are invariant to the inclusion of points for which there are no errors. The space carving approach employed here has no false negatives and as such, the values are the same as if the error metric were applied to the state vector.

425

4.1 Extinction retrieval

Let us first consider the robustness of the results to noise before interpreting them in detail. The accuracy of the Default and Low retrievals using noise free measurements are shown in Table 1. The ensemble-averaged error metrics with respect to the ground truth differ by less than 1% between the noise free retrievals (Default and Low) and the noisy retrievals (Default-**Noisy** and Low-**Noisy**). For this reason, we do not report the retrieval accuracies for the Default-**Noisy** and Low-**Noisy** retrievals. Instead, we report their differences with respect to the noise free retrievals (Table 2). Additionally, we found that the retrieval errors of the **Noisy-GroundTruth** retrievals were less than 0.01% for all realizations in all cloud categories so we do not report further details of the results of those retrievals. Immediately, we can see that the ensemble-averaged results are robust to the inclusion or exclusion of noise.

430

435

The differences between the noisy and noise free retrievals increase with optical depth (Table 2) and can include large systematic differences between retrievals for particular realizations in the Thick and Very Thick cloud categories. This latter feature can be seen in the large ranges of the error metrics in Table 2 for the Very Thick cloud category. The large deviations between noise free and noisy retrievals indicates large uncertainties in these retrievals. The differences in between the Default/Low retrievals and their corresponding noisy variants (Table 2) are much larger than the retrieval errors of the **Noisy-GroundTruth** retrievals (which are negligible). This large discrepancy indicates that the issues of non-linearity and errors in the local optimization will confound uncertainty quantification as ensemble-based uncertainty estimates will differ depending on the choice of initialization. We revisit the implications of this point in the Discussion (Section 5). We focus the rest of our analysis on explaining the variability in retrieval accuracy for the noise free retrievals.

440

445

Table 1: Extinction Errors for the different retrieved clouds in each category. Means of error metrics are shown across the 10 clouds in each category with the standard deviation across the 10 clouds in parentheses. See text for details of the error metrics.

Inversion Method	Default				Low				20 th Low iteration Restart		Final Low iteration Restart	
	Thin	Medium	Thick	Very Thick	Thin	Medium	Thick	Very Thick	Thick	Very Thick	Thick	Very Thick
Relative RMSE (%)	14.6 (1.7)	19.3 (2.9)	45.8 (7.4)	73.0 (2.7)	24.6 (1.5)	37.3 (3.1)	53.3 (4.8)	63.2 (4.3)	42.4 (4.4)	62.7 (3.6)	49.0 (6.5)	62.7 (4.5)
Relative Bias (%)	0.2 (0.1)	0.1 (0.1)	-6.6 (6.6)	-35.6 (9.5)	3.2 (1.4)	5.0 (2.5)	8.4 (6.2)	-7.5 (13.7)	-0.5 (3.3)	-14.7 (12.1)	4.2 (5.6)	-8.3 (13.7)
Relative Bias in coefficient of variation (%)	-2.2 (0.5)	-3.5 (0.8)	-9.5 (4.3)	-18.4 (8.1)	-7.6 (1.4)	-9.2 (2.8)	-7.2 (2.6)	-6.0 (7.1)	-8.4 (1.8)	-8.9 (4.8)	-6.5 (2.2)	-5.8 (7.3)

450 **Table 2: Differences between the extinction fields from noisy and noise free retrievals. Means of error metrics are shown across the 10 clouds in each category with the minimum and maximum across the 10 clouds in parentheses. See text for details of the error metrics.**

Inversion Method	Default-Noisy				Low-Noisy			
	Thin	Medium	Thick	Very Thick	Thin	Medium	Thick	Very Thick
Relative RMSE with respect to Noise Free retrieval (%)	2.4 (1.9, 3.3)	3.6 (1.5, 6.15)	24.5 (5.4, 51.2)	30.1 (6.3, 51.9)	2.1 (1.5, 2.9)	3.4 (0.8, 7.4)	6.7 (1.7, 13.3)	16.8 (4.2, 36.6)
Relative Bias with respect to Noise Free retrieval (%)	0.0 (-0.05, 0.04)	0.0 (-0.05, 0.04)	-3.1 (-17.5, 5.3)	2.8 (-12.6, 16.5)	0.0 (-0.04, 0.03)	-0.1 (-0.38, 0.1)	0.0 (-1.7, 1.6)	-1.0 (-11.4, 8.5)

The Default retrievals for the Thin and Medium cloud categories are uniformly accurate, with negligible bias and small relative RMSEs (Table 1). The Low retrievals have lower accuracies than the Default retrievals for these two categories due to their large forward modelling error. The cost function of the Low retrievals for the Thin and Medium cloud categories (Fig. 3) begins to decrease very slowly with iteration number after only around 20 iterations and asymptotes to a larger value than for the Default retrievals. The local optimization can proceed for ~100 iterations for the Default retrievals in the Thin and Medium cloud categories. However, the results for the Low retrievals indicate that retrievals may converge within much fewer iterations for these clouds in the presence of modelling and instrumental errors. Given the good performance of the Default retrievals, we do not consider any Restarted retrievals for the Thin and Medium cloud retrievals. The worse performance of the Low retrieval indicates no benefit from the better conditioning and more accurate Jacobian approximation for these clouds.

455

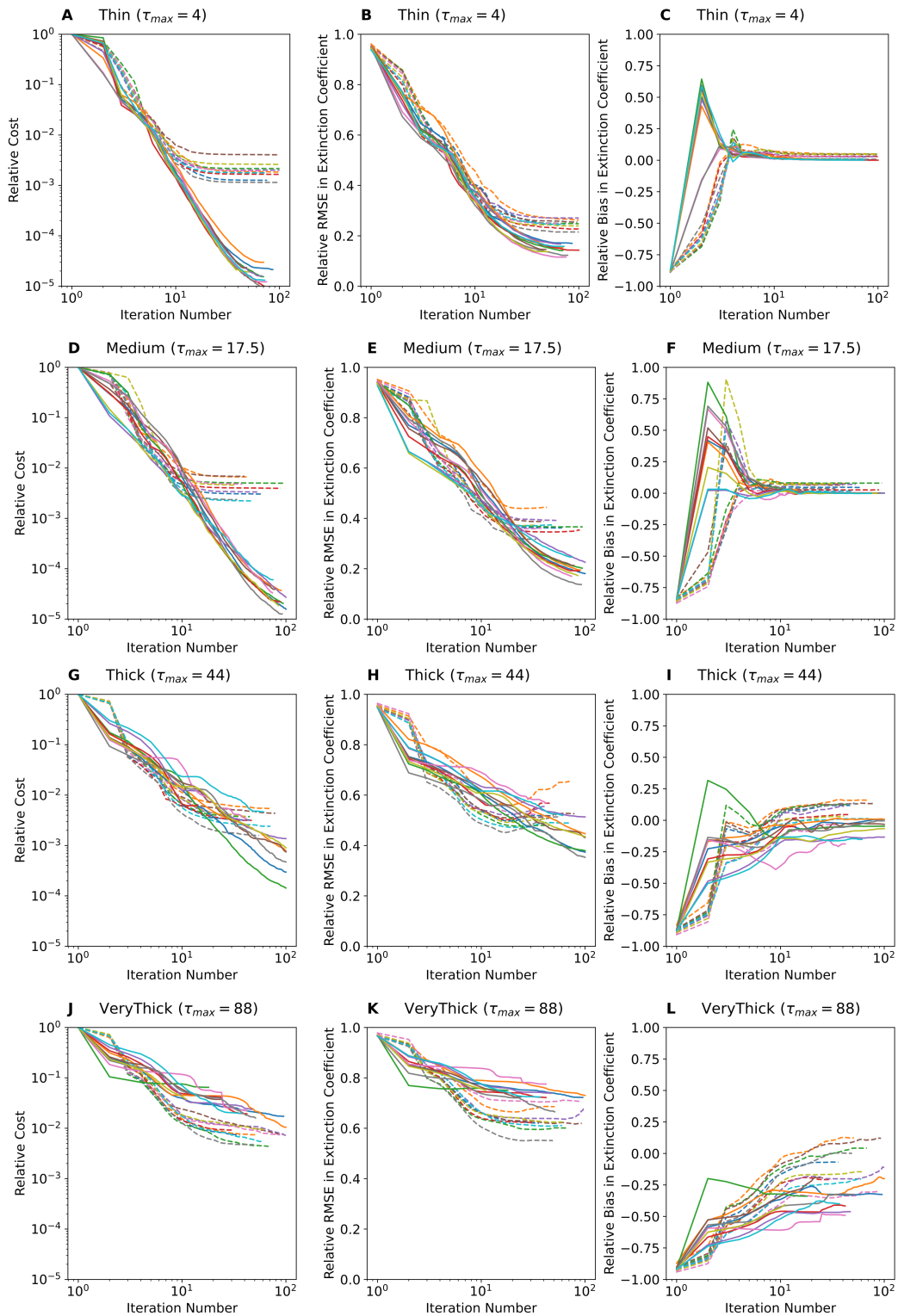
460

The accuracy of the retrievals systematically degrades with increasing optical depth. The rate of reduction of the cost function
465 with iteration number decreases as the optical thickness of the clouds increases (Figure 3), which can be seen by comparing
the behaviour of the Medium, Thick and Very Thick cloud categories. Relative RMSE systematically increases with optical
depth (Table 1) for both the Default and Low retrievals and a large bias of -36% develops in the Default retrievals in the Very
Thick category. This bias is dramatically reduced to just -7% in the corresponding Low retrievals. The convergence behaviour
470 of the Low retrieval for the Very Thick clouds (Figure 3L) shows that the Low retrieval more rapidly increases the mean
extinction with iterations particularly beyond 10 iterations, where the cloud has become optically thick. The final cost functions
obtained by the Low retrievals are much lower than the Default retrieval. This is associated with a lower relative RMSE in the
final modelled radiance fields of just 9% when compared to 16% for the Default retrieval. The differences between the Default
and Low retrievals for the Thick clouds are milder but are still significant, with a lower relative RMSE and slight improvements
in the bias.

475

The dramatic improvement in the reported accuracies of the Low retrieval for the clouds in the Very Thick category indicates
that there is a substantial sensitivity of the retrieval to the choice of angular resolution in the forward model. The apparent
benefit of using the Low accuracy retrieval is carried through into both types of Restarted retrievals. Using the high accuracy
forward model in the Restarted retrieval does little to improve the retrieval accuracy beyond that of the Low retrieval used to
480 initialize it (Table 1). This indicates that the local optimization algorithm is unable to further reduce the residuals despite the
use of a more accurate forward model.

The faster convergence of the mean of the Low retrieval, when compared to the Default retrieval in the Very Thick category
(Figure 3L) is suggestive that it is the better conditioning of the forward model that drives the improvement in the convergence.
485 However, the improvement in the retrieval accuracy may be due to compensating biases in the approximate forward model.
To help us distinguish between these effects we make use of the results of the Low-GT retrievals (Table 3). These retrievals
are initialized with the ground truth cloud, but use the Low accuracy forward model. The resulting retrieval errors are therefore
a local estimate of the error in the retrieved state due to forward modelling errors in the vicinity of the ground truth. The
retrieval error for the Low-GT Thin and Medium clouds are similar to those of the standard Low retrieval. This further solidifies
490 the good behaviour of the retrievals in these cloud categories.



495 **Figure 4: Retrieval performance for the Default (solid lines) and Low (dashed lines) retrievals as a function of iteration number for clouds in the Thin (A, B, C), Medium (D, E, F), Thick (G, H, I) and Very Thick (J, K, L) categories. Each coloured curve corresponds to a different cloud realization. The first column (A, D, G, J) shows the cost function normalized by its initial value. The second column (B, E, H, K) shows the relative RMSE (Eq. 6) in the retrieved volume extinction coefficients. The third column (C, F, I, L) shows the relative bias (Eq. 7) in the retrieved volume extinction coefficient. See main text for details of the error metrics. Note the logarithmic scale of the iteration number, given that computational expense is linear in iteration number.**

500 **Table 3: Extinction Errors for the Low-GT retrievals. Means of error metrics are shown across the 10 clouds in each category with the standard deviation across the 10 clouds in parentheses. See text for details of the error metrics.**

Inversion Method	Low-GT			
Cloud Category	Thin	Medium	Thick	Very Thick
Relative RMSE (%)	15.6 (1.6)	27.7 (2.8)	38.1 (8.0)	18.6 (6.4)
Relative Bias (%)	3.1 (1.4)	5.0 (2.5)	10.2 (5.2)	6.2 (4.4)
Relative RMSE with respect to the Low retrieval. (%)	17.8 (1.8)	22.2 (2.2)	34.8 (4.1)	68.6 (12.6)
Relative Bias with respect to the Low retrieval (%)	-0.1 (0.0)	-0.1 (0.2)	1.8 (1.8)	16.9 (14.7)

505 The relative bias of the Low-GT retrieval for the Thick cloud category is 10.2% in the ensemble average (Table 3). This shows that much of the difference between the relative Bias in the Default and Low retrievals can be explained by the forward model error. In particular, the Low accuracy model produces smaller radiances for a given optical thickness of the cloud, so the cloud must be biased high in optical thickness to minimize misfit against the measured radiances. The retrieval bias of the Low-GT retrieval in the Very Thick clouds is only 6.2%. This is much smaller than the difference in relative bias between the Default retrieval and the Low retrieval. As such, forward model error in the vicinity of the solution cannot entirely explain the discrepancy between the two techniques. Part of this discrepancy is caused by the fact that the Default retrieval does not converge to the vicinity of the truth in terms of average extinction and so the forward model error at the ground truth is not representative. However, the bias difference is still much larger than the 10.2% bias that occurs for the Thick category. The other component of the difference between the Default and Low retrievals is because the trajectory of the local optimization from the optically thin initialization to the final retrieved state is very different.

515 To better understand the differences in the optimization trajectories between retrievals that use different forward models let us examine the spatial structure of the extinction errors. Understanding the character of these errors is important for us to understand how to mitigate these errors, particularly in the optically thick limit and whether a low accuracy, **better-conditioned**

less ill-conditioned, forward model may be a part of a mitigation strategy. In doing so, we explain how such a biased extinction field can be retrieved that still provides a relatively small misfit against the radiance measurements in the optically thick limit.

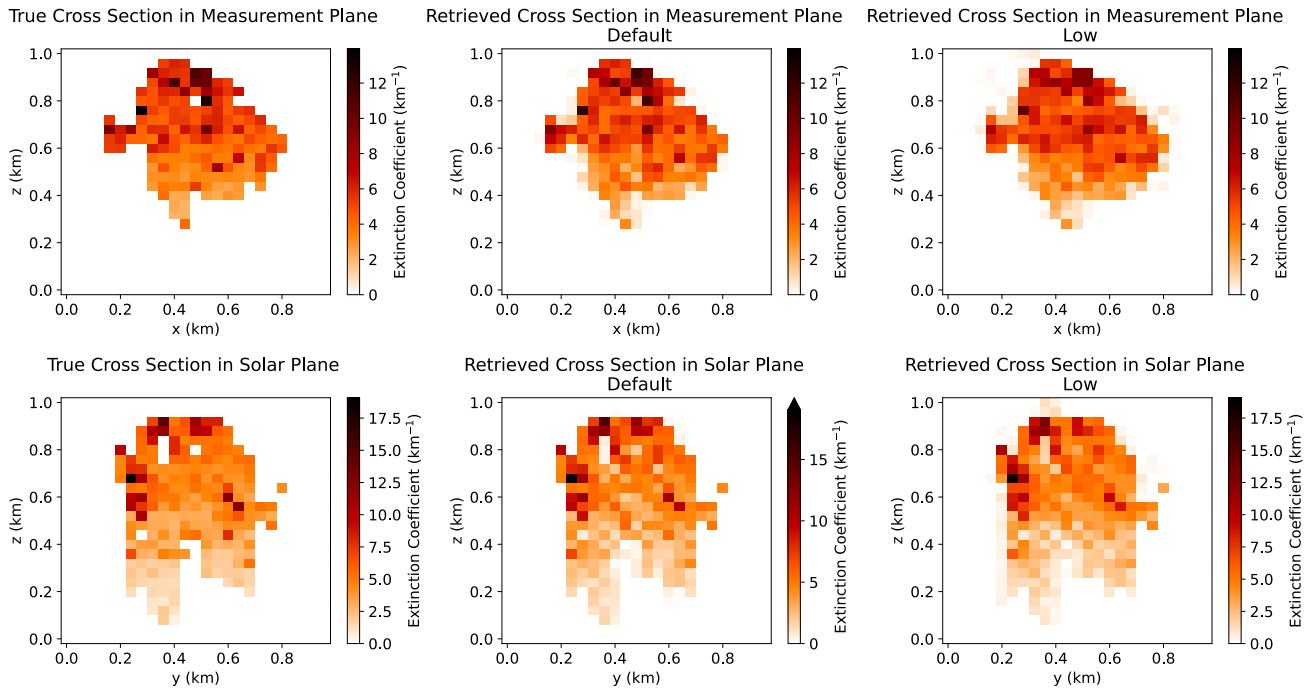
520 As a starting point in our analysis of the spatial structure of the retrieval errors let us note that all retrievals have underestimated the variability in the retrieved extinction field, especially at larger optical depths in the Default retrieval. This is demonstrated through the errors in the coefficient of variation of the extinction field (Table 1). We further examine the spatial dependence of this error by examining cross sections of the retrieved extinction field. In Figures 4 to 7 we show cross-sections of the volume extinction coefficient for cloud realization #4 of the stochastic clouds as it is representative in providing all of the key
525 points from the other realizations when visualizing the spatial structure of the errors. We show just the Default and Low retrievals as the Restarted retrievals are qualitatively similar to the Low retrievals. Cross sections of the extinction field are shown for the slices through the centre of the domain aligned along the azimuthal directions of the sensors and the sun. We refer to these slices as the measurement plane and solar plane, respectively.

530 The high-frequency details of the extinction field are retrieved almost perfectly for the Thin (Fig. 4) and Medium (Fig. 5) clouds, with only mild errors apparent in the measurement plane of the Medium cloud. On the other hand, for the Thick (Fig. 6) and Very Thick (Fig. 7) clouds, the extinction field is extremely smooth. There is a gradient in extinction in the solar plane from the illuminated side (left) to the shaded side (right) of the retrievals of the Thick and Very Thick clouds. Fine details of the extinction field are retrieved on the illuminated side, but not on the shadowed side. Additionally, the largest values of the
535 retrieved extinction tend to be at the edge of the cloudy volume (as defined by space carving) in the measurement plane with the smallest values in the centre. This feature is most apparent in the Default retrievals.

To examine the scale-by-scale apportionment of the error across the whole ensemble of retrievals, we use Fourier analysis. Fourier analysis is a global analysis so it cannot identify, for example, a lower error in small-scale features on the illuminated
540 side of the cloud. To compress the information, we show just the isotropic, ensemble averaged power spectral density of the retrieved extinction fields (Fig. 8) and their errors (Fig. 9). The retrievals tend to be significantly smoother than the ground truth at small scales. The scale below which the retrieval has less variability than the truth increases from 125 m to 250 m as the clouds become optically thicker. Note that the default retrieval for the Very Thick clouds tends to underestimate variability at all scales, an error that is reduced in the Low and Restarted retrievals consistent with the reduction in the underestimate of
545 variability (Table 1). Note that the reproduction of approximately correct power spectra at large scales doesn't necessarily indicate that the retrievals are error free at these scales, since the phasing of the spatial modes can still disagree and lead to error proportional to the amplitude of the mode.

The errors in the Default retrievals of the extinction for the Thin and Medium cloud categories are actually band-limited to
550 small scales (Fig. 9). Errors tend to occur primarily at larger scales for the other retrievals, especially in the Thick and Very

Thick categories. This indicates that even large-scale features are not accurately retrieved in the Thick and Very Thick clouds, in general, in concurrence with Fig. 6 and Fig. 7. The primary benefits of the Low and Restarted retrievals in terms of overall reduction of RMSE are felt at the largest spatial scales (Fig. 9).



555 **Figure 5:** Vertical cross sections of the true extinction field (Left), Default retrieved extinction field (Middle) and the Low retrieved extinction field (Right) for Cloud #4 in the Thin category. Cross sections are in the $y = 0.48$ km plane (Top) and the $x = 0.48$ km plane (Bottom). The sun points in the positive y direction, while the viewing directions are aligned along the x axis.

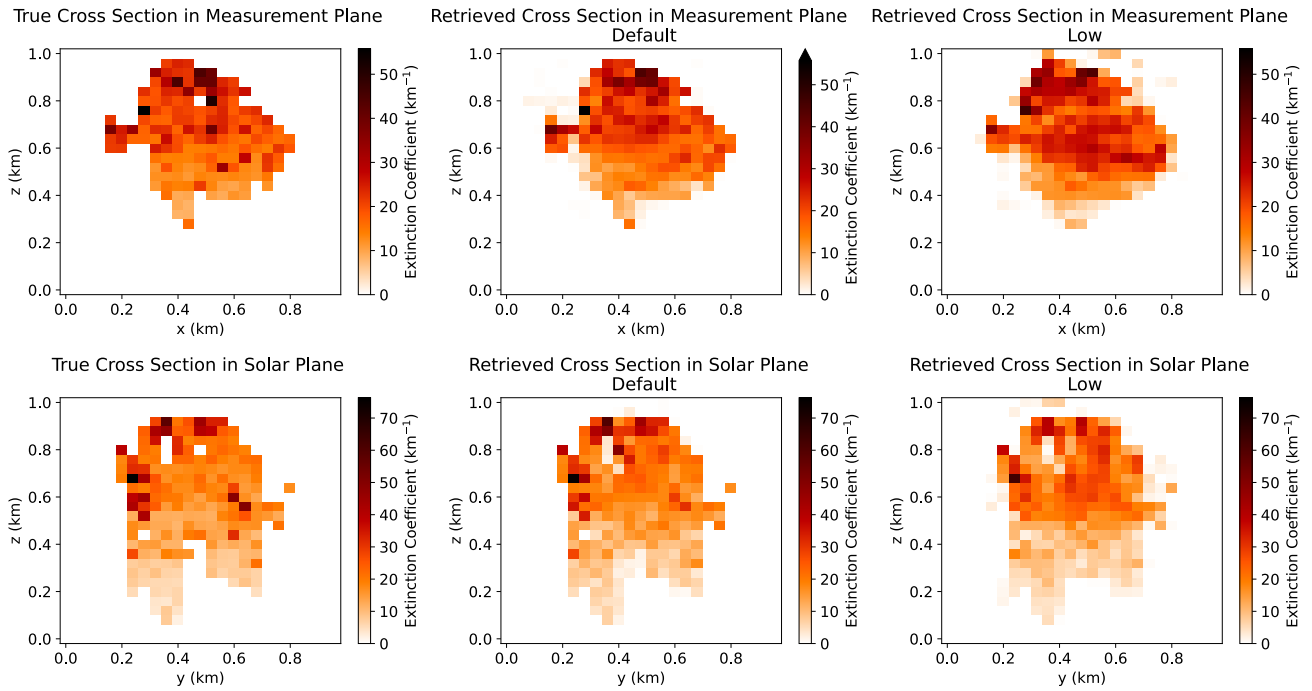


Figure 6: As in Figure 4 but for the Medium cloud category.

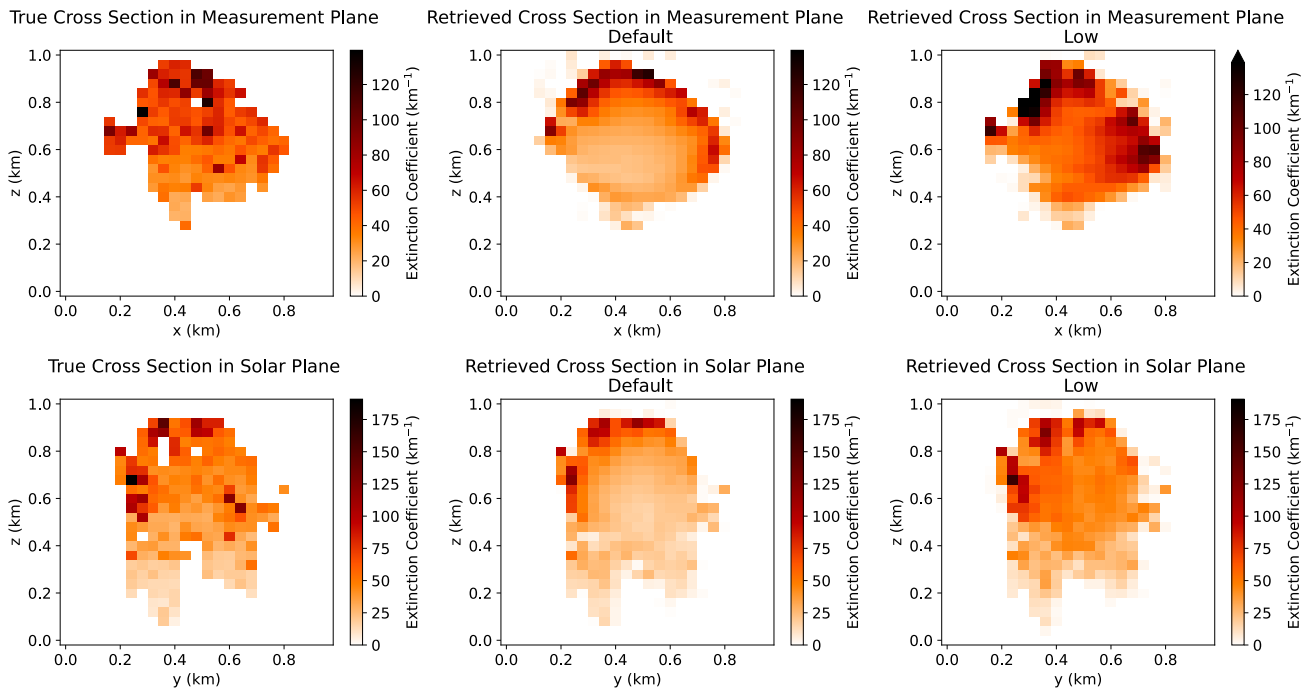


Figure 7: As in Figure 4 but for the Thick cloud category.

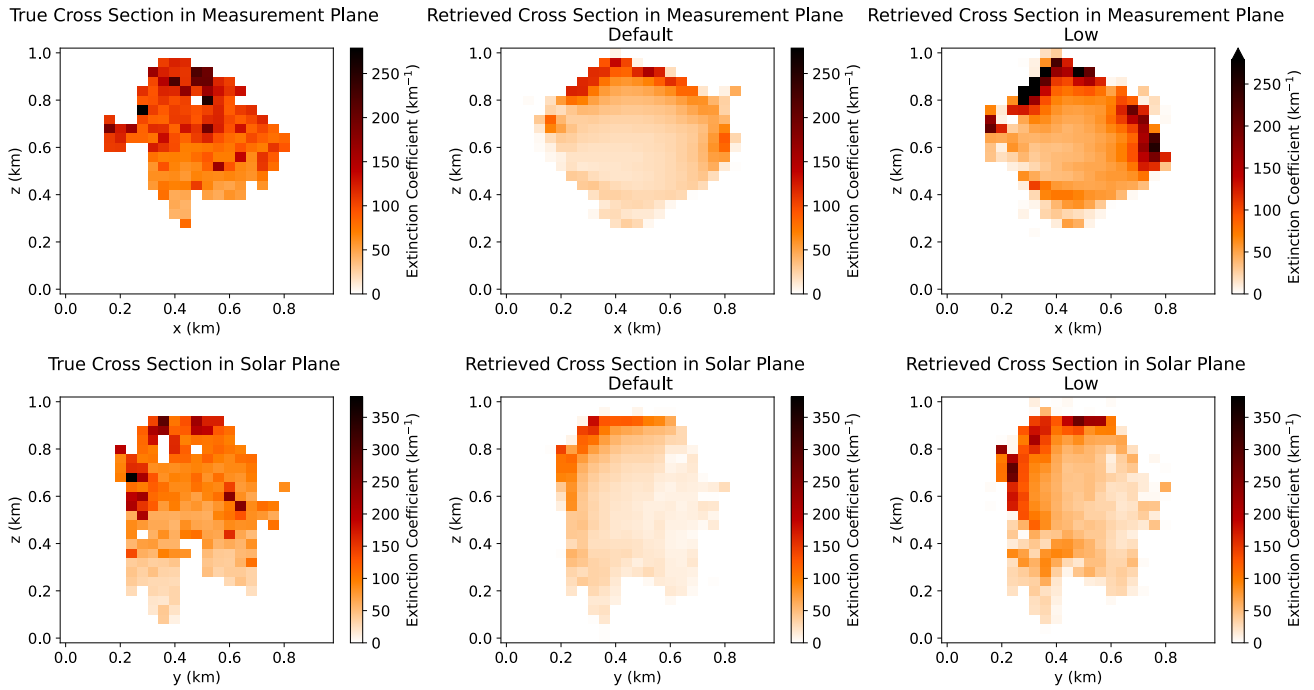
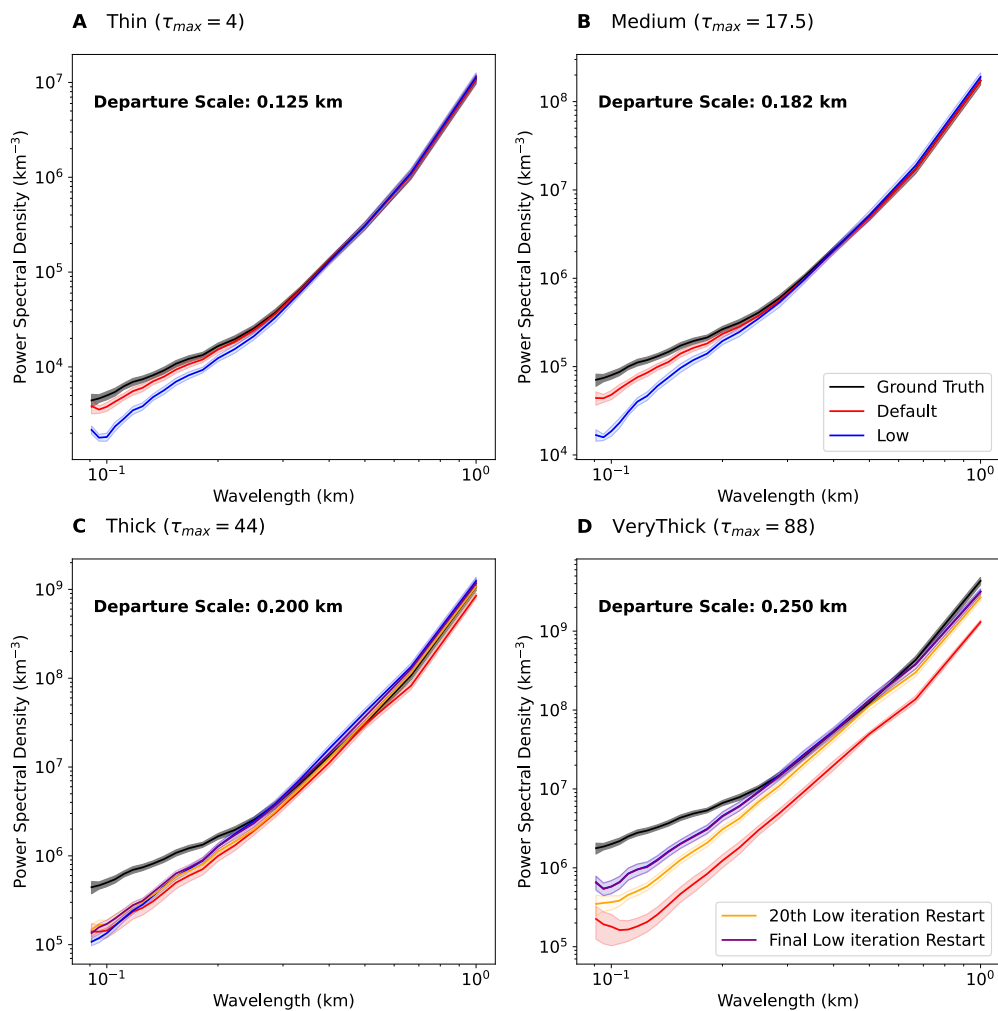


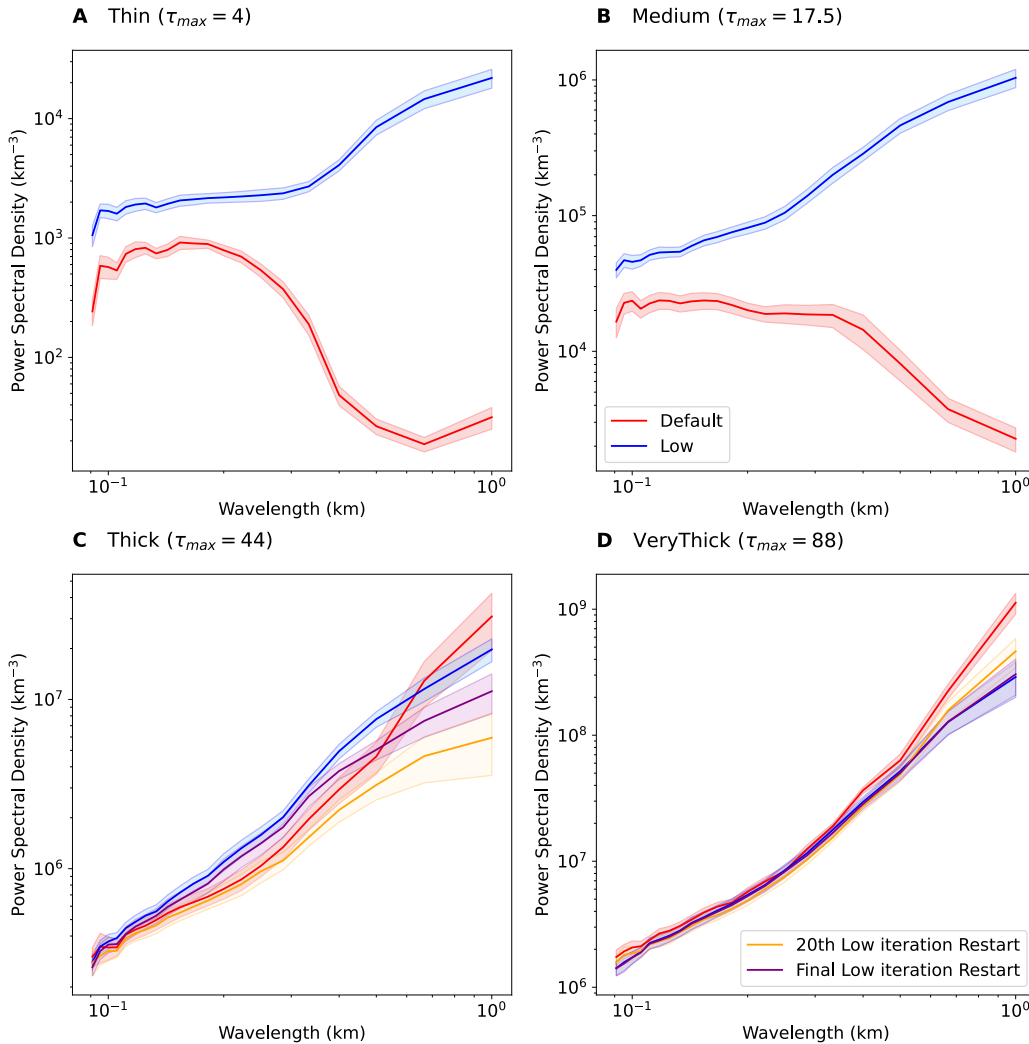
Figure 8: As in Figure 4 but for the Very Thick cloud category.



565

Figure 9: The ensemble averaged, isotropically averaged power spectral density of the volume extinction coefficient for the Thin (A), Medium (B), Thick (C) and Very Thick (D) cloud categories. Solid lines are the ensemble averages, and the shading indicates \pm one standard error in the mean. The spatial scales of the first departure from the ground truth spectrum by the best performing retrievals for each cloud category are marked in the top left corners of each figure. Note in panel D, the Low and Restarted Final curves are indistinguishable.

570



575 **Figure 10: The ensemble averaged, isotropically averaged power spectral density of the errors in the volume extinction coefficient for different retrievals of the clouds in the Thin (A), Medium (B), Thick (C) and Very Thick (D) categories. Solid lines are the ensemble averages, and the shading indicates +/- one standard error in the mean. Note in panel D, the Low and Restarted Final curves are indistinguishable.**

The spatial structure of the retrieval error for the Default and Low retrievals of the clouds in the Thick and Very Thick categories for the naïve, optically thin initialization, give us some important insight into some of the issues that arise in retrievals of optically thick clouds. The details of the spatial structure of the error in our retrievals are unique to our choice of initialization. In the discussion below, we distinguish between the explanation of our retrieval errors and hypotheses that we
 580 make about the general behaviour of the local optimization in the optically thick limit.

For our particular retrievals, the optically thick cloud state is approached from an optically thin cloud state. During the early iterations, the residuals are highly smooth as we initialize with an extremely optically thin cloud. As such, the optimization updates the cloud by reducing the bias in the radiances and fills the cloud with a relatively smooth extinction field. As the bias
585 reduces, the cloud becomes optically thick and now the optimal strategy to reduce the cost function is to further increase the extinction on the illuminated side of the cloud and at the cloud edge in the plane of the measurements. This patterning is because the magnitudes of the Jacobian elements are largest in these positions, as described in detail in Part 1. With the bias in the cost function reduced, the radiance residuals can be multi-signed and mapped more strongly to smaller-scale spatial features in the extinction field. However, the cloud is now optically thick and this mapping is highly ill-conditioned. So, it is
590 difficult from a linearized perspective to redistribute extinction between the outer and inner portions of the cloud while avoiding an increase in the cost function. Tiny step sizes must be utilized to avoid instability, but even these are corrupted by the increasing error in the approximate linearization. Eventually, cost function reductions are so small that the stopping condition of the optimization is achieved. This results in the presence of gradients in cloud extinction from illuminated to shadowed side and from cloud edge to cloud core in the retrieved state.

595

Based on the behaviour of the retrievals, we argue that the improvement of the Low retrieval relative to the Default retrieval for these Very Thick clouds is driven by the better conditioning of the forward model. The ratio of the magnitude of the Jacobian elements tends to be more similar between cloud edge and cloud centre, and the illuminated and shaded sides of the cloud for the ~~better-conditioned~~ **less ill-conditioned**, low accuracy forward model (Loveridge et al., 2022b). The result of this
600 is that the extinction is distributed more evenly throughout the cloud during the increase in the extinction coefficient even at larger optical depths.

The smoothness of the extinction field in our retrievals (e.g. the coefficient of variation in Table 1) arises because of the smoothness of the initial residuals and the smoothing effect of the adjoint operator that is used to calculate the gradient. The
605 solution operator of the radiative transfer is smoothing and so is its adjoint. In the ill-conditioned limit, local optimization tends to converge slowly while remaining smooth. This contrasts with direct inversion methods that can produce wild irregularities in the solution when the problem is ill conditioned. The greater smoothness of the Default retrieval for the Very Thick clouds, compared to the Low retrieval, can be seen as a symptom of the stronger ill-conditioning that occurs in the Default retrieval before details in the extinction field are retrieved.

610

The smooth extinction fields that we retrieved in the optically thick limit that are biased low are only one of a set of configurations of clouds that will produce similar consistency in radiances against the measurements. Compensating errors in the radiance field occur between biases in the mean and the variability of a retrieved extinction field. This is because a low bias in extinction increases the mean-free-path, hence enhancing transmission, while decreasing spatial variability decreases
615 the mean-free-path, hence decreasing transmission (Cairns et al., 2000; Davis and Marshak, 2004; Forster et al., 2021). These

compensating errors can be larger in optically thick clouds without substantially affecting the outgoing radiance field due to the strong smoothing process of scattering (Davis et al., 2021).

620 We must emphasise that our results are not evidence of a radiative smoothing bias in tomographic retrievals similar to the one identified in the IPA. The resolving power of the measurements is affected by not just the spatial resolution but also the angular spacing of the measurements. In the optically thick limit, there is an ambiguity in the state when using only radiance measurements in the retrieval. The smoothness of our retrieved extinction fields is an artefact of our choice of retrieval algorithm (and particularly its initialization). Retrievals with other initializations may encounter the opposite form of compensating error. For example, a retrieval may be initialized optically thick and highly variable, which results in the retrieved
625 cloud being too optically thick and too variable. At this point, this is a hypothesis about the general behaviour of retrievals in the optically thick limit and remains to be tested.

4.2 Inferred optical depths

In addition to the analysis of the volume extinction coefficient field, it is also helpful to consider how the retrieval performs for inferring optical and radiative properties such as cloud optical depth. Cloud optical depth is a widely used single variable
630 for describing the optical properties of cloud and, for this variable, we can make a direct comparison with the performance of operational retrievals using 1D RT.

Table 4 shows the retrieval errors in optical depth distributions from the different tomographic retrievals. Retrieval errors in optical depth are substantially smaller than in the extinction field, reflecting the relatively uncorrelated spatial distribution of
635 extinction errors. For comparison, Table 5 displays retrieval errors from an optical depth retrieval using only nadir radiance and the assumptions of the IPA, that is, using homogeneous plane-parallel cloud models and 1D RT to generate look-up tables (LUTs) of optical depth as a function of measured radiance. Errors are substantial for the IPA retrieval, even with radiances at the same resolution as the optical depth so that sub-pixel heterogeneity effects are absent. The IPA retrieval outperforms the default tomographic retrieval of the Very Thick clouds, but the margin is well within the ensemble standard deviations of both
640 techniques. Moreover, even accounting for the ensemble variability, the IPA is significantly out-performed by both Restarted retrievals, which have small radiance residuals. The tomographic retrieval also outperforms the IPA retrieval when inferring the coefficient of variation of the optical depth distribution as the IPA retrieval tends to have a bias in the estimate of the distribution width that changes sign with increasing optical depth (Iwabuchi and Hayasaka, 2002). Clearly, the tomographic retrieval demonstrated here is much more appropriate for inferring cloud optical depths in cumuliform clouds than IPA-based
645 retrievals, even without considering the substantial benefits of retrieving the 3D distributed extinction field.

Table 4: Optical Depth Errors for different tomographic retrievals. Means of error metrics are shown across the 10 clouds in each category with the standard deviation across the 10 clouds in parentheses. See text for details of the error metrics.

Inversion Method	Default				Low				20 th Low Iteration Restart		Final Low Iteration Restart	
	Thin	Medium	Thick	Very Thick	Thin	Medium	Thick	Very Thick	Thick	Very Thick	Thick	Very Thick
Relative RMSE (%)	2.8 (0.5)	7.2 (1.6)	24.1 (6.1)	55.6 (4.1)	8.1 (1.2)	17.7 (3.2)	28.5 (5.4)	36.5 (5.0)	19.9 (2.2)	38.8 (4.7)	24.5 (5.9)	36.4 (5.4)
Relative Bias (%)	0.2 (0.1)	0.0 (0.1)	-6.6 (6.6)	-35.6 (9.5)	3.2 (1.4)	5.0 (2.5)	8.3 (6.1)	-7.6 (13.7)	-0.5 (3.3)	-14.7 (12.1)	4.1 (5.6)	-8.3 (13.7)
Relative Bias in coefficient of variation (%)	-0.1 (0.1)	-0.7 (0.4)	-4.8 (1.3)	-14.0 (6.0)	-2.6 (0.9)	-1.6 (1.6)	0.1 (2.8)	-3.2 (3.0)	-1.9 (1.2)	-5.0 (3.7)	-0.3 (2.3)	-3.3 (3.3)

650 **Table 5: Optical depth errors for a Look Up Table (LUT) based retrieval of optical depth from the nadir radiance using 1D radiative transfer. Means of error metrics are shown across the 10 clouds in each category with the standard deviation across the 10 clouds in parentheses. See text for details of the error metrics. The LUT uses the ground truth microphysics and is made of 20 points with linear spacing between 0 and 5 optical depths and 40 points with logarithmic spacing between 5 and 100. A cubic interpolation is used. The best fitting optical depth is chosen using the L-BFGS-B routine. The angular accuracy used to form the LUT is the same as the ground truth 3D simulations but a stricter splitting accuracy of 10^{-3} is used.**

Inversion Method	IPA / LUT			
	Thin	Medium	Thick	Very Thick
Relative RMSE (%)	29.4 (2.7)	38.9 (4.8)	45.7 (6.2)	78.7 (14.1)
Relative Bias (%)	-23.2 (2.7)	-31.9 (4.5)	-31.9 (10.3)	-16.9 (25.0)
Relative Bias in coefficient of variation (%)	-7.4 (1.8)	-7.0 (3.4)	1.7 (7.9)	31.2 (15.7)

655

4.3 Computational expense

As always, it is important to also consider the computational expense of a retrieval method alongside its performance when evaluating its utility. Table 6 evaluates the computational expense of the retrievals. It shows that the use of the low accuracy SHDOM solver in the Low retrieval almost eliminates the contribution of the RTE solver to the retrieval time, which is instead dominated by the approximate computation of the gradient and radiance calculation. This latter calculation is still unoptimized, and its cost is further discussed in Appendix F of Part 1 (Loveridge et al., 2022b). The gradient calculation is easily parallelized using multi-threading as each observable can be evaluated independently. In our case, we parallelize using 4 threads. True

660

CPU time is therefore roughly four times larger than wall-time for this portion of the computational cost of each iteration. Computational expense is, naturally, significantly larger for the tomographic retrieval than for the IPA-based retrieval. For comparison, the tomographic retrieval is, very roughly, two orders of magnitude more expensive than aerosol retrievals using multi-angle radiances and the IPA assumptions with online RTE calculations, neglecting differences in hardware (Gao et al., 2021).

Table 6: Computational Expense of the Retrievals. Means across the ten clouds are shown, with standard deviations across the ten clouds in parentheses. Average cumulative Total CPU time is essentially linear in iteration number so the computational expense vs. accuracy trade-off of terminating the retrievals earlier can then be read from this Table and Figure 3. All computations were performed on a 2.3 GHz Intel Core i5.

Inversion Method	Default				Low			
	Thin	Medium	Thick	Very Thick	Thin	Medium	Thick	Very Thick
Total CPU Time per iteration (s)	43.6 (7.3)	53.2 (10.9)	85.8 (8.5)	115.9 (48.8)	29.6 (6.1)	31.6 (10.0)	36.3 (13.1)	30.2 (6.5)
Percentage of Total CPU time spent on SHDOM solution (%)	20.4 (1.6)	43.7 (5.2)	54.5 (6.6)	57.0 (7.1)	0.5 (0.1)	1.2 (0.2)	2.3 (0.2)	3.6 (0.6)
Average number of Objective Function Calls per iteration	1.60 (0.27)	1.17 (0.15)	1.30 (0.27)	1.50 (0.58)	1.58 (0.39)	1.82 (0.56)	1.83 (0.69)	1.47 (0.29)

Several acceleration methods are possible. The computational scaling of the SHDOM solver to larger domains using MPI-based parallelization is documented in Pincus and Evans (2009). The solver CPU time may be decreased by using the SHDOM solution from the previous optimization iteration to initialize the next one. We utilized this feature in Part 1 to accelerate finite differencing calculations, though this method may not be stable to large changes in cloud between iterations, particularly when the adaptive grid is utilized. A more sophisticated version of this principle is to utilize PDE-constrained optimization which jointly refines both the inverse problem and the RTE solution at the same time, leading to order of magnitude decreases in computational expense (Abdoulaev et al., 2005). The use of low accuracy RTE solutions far from the solution appears valuable, through their ability to reduce the computational expense of the solver and increasing the convergence rate of the optimization.

The RTE solver cost may be mitigated in operational applications through the development of a statistical emulator for the SHDOM RTE solution similar to Gao et al. (2021), though this work should likely proceed only once the retrieval algorithm is at a greater level of maturity. The convergence rate of the retrieval, and hence total computational expense, and final accuracy may also be improved through the development of preconditioning strategies. The problem of ill-conditioning in the transition to the diffuse regime has been widely recognized in Diffuse Optical Tomography and some mitigation strategies have been

proposed (Tian et al., 2010; Niu et al., 2010). Extension of this work for a nonlinear preconditioning transform (De Sterck and Howse, 2018) may be effective for our application. In our view, the computational expense of the tomography retrieval is not an oppressive limitation of the technique. Significant computational resources are routinely utilized simply to simulate analogues of the atmospheric system. The technique only calls for similar resources to be directed to study the atmosphere as it really is.

5 Discussion

The good performance of the retrievals of the clouds in the Thin and Medium categories is highly encouraging, as is their robustness to noise and their robustness to forward model error in this idealized scenario. Clearly, in these clouds, the approximate Jacobian is not a limiting factor in the local optimization, and the local optimization itself is a highly efficient method for performing the retrieval. While we must be careful not to extrapolate quantitative performance from our idealized scenario to real world conditions, we can confidently conclude that the performance of the tomography for isolated clouds within this scattering regime will be limited by forward modelling error and instrumental errors, rather than the difficulty of the inverse problem. Given that many trade cumulus tend to be smaller than 800 m in geometric depth (Guillaume et al., 2018; Chazette et al., 2020) and that the average adiabatic fractions for these clouds can be significantly less than unity (Eytan et al., 2022), many of these clouds, particularly in clean-conditions will confidently have maximum optical depths less than 40.

A minimal amount of prior information will be required to perform retrievals of these optically thinner shallow cumulus. In fact, our results cement the conclusion that small heterogeneous clouds are actually the clouds for which remote sensing using passive imaging is easiest, counter to the paradigm of 1D radiative transfer. This means that the radiance measurements themselves will provide a large amount of information that is independent of the models that might be used to form any priors such as LES. This is hugely encouraging as the development of cloud tomography techniques is motivated in part by the need to develop measurements that provide independent constraints on the behaviour of LES models (Morrison et al., 2020). This fact solidifies the strengths of physics-based retrievals in comparison statistical methods. While statistical methods trained using LES data are also attractive options to perform retrievals using 3D radiative transfer (Nataraja et al., 2022; Ronen et al., 2022), they lack a ground truth training data set and are not independent of the LES that they may be used to evaluate.

One of the key issues that might complicate our extrapolation of tomography performance to real clouds is the potential for cloud organization to obscure oblique views and thereby lower retrieval accuracy. Additionally, there is the issue of how the retrieval accuracy depends on the treatment of the horizontal boundary conditions and domain size. These issues have yet to be investigated systematically, requiring much larger domains, hence computational expense, and therefore MPI-based parallelization, which is not yet implemented in AT3D. Observed statistics of cloud-to-cloud separation suggest that trade cumulus are tightly spaced relative to their horizontal size, and therefore thickness (Zhao and Di Girolamo, 2007). Early numerical results of radiative transfer with idealized cloud geometries show that the radiative effects of cloud-cloud

interactions are significant in this regime (Weinman and Harshvardhan, 1982; Schmetz, 1984; Kobayashi, 1988). As such, investigating the sensitivity of the retrieval accuracy to cloud-cloud interactions, particularly the horizontal boundary conditions, is a high priority for establishing the efficacy of cloud tomography in more realistic conditions.

725 Given the success of the local optimization and approximate Jacobian in the optically thin limit, the proposed retrieval is also
applicable to other optically thin scattering media such as cirrus or aerosol. For cirrus clouds, the primary barrier will likely
be whether the clouds have sufficient horizontal variability for the multi-angle measurements to constrain their vertical
structure. Horizontal homogeneity increases ill-conditioning, introducing ambiguity in the retrieved extinction fields (Martin
and Hasekamp, 2018), though this effect is relatively minor in the optically thin limit (Loveridge et al., 2022b). Additionally,
730 the more complex microphysical characteristics of ice and aerosols, where the shape and composition are not well known a
priori, raises the question of how effective microphysical retrievals for these scatterers will be. In contrast, tomographic
retrievals of liquid cloud microphysics have already been demonstrated (Levis et al., 2020) and promise to be effective in the
optically thinner cumuliform clouds discussed above.

735 In the optically thick limit, many issues have been identified. We have provided further quantification of the degradation of
retrieval accuracy and convergence in the optically thick limit due to ill-conditioning that had been previously identified (Levis
et al., 2015; Martin and Hasekamp, 2018). Retrieval uncertainties are clearly large in the optically thick limit, as indicated by
the significant divergences of the retrieved extinction field due to small perturbations to the measurements. However, even
these perturbative estimates are tied to our choice of initialization and are not globally representative (Rodgers, 2000; Gao et
740 al., 2022). We showed that while we can easily diagnose retrieval accuracy using the ground truth, we currently have no
effective means to predict retrieval uncertainties. Developing a computationally efficient uncertainty model is a critical step in
the development of the tomographic retrieval. Particle filter methods have the potential to address this need (Hu and van
Leeuwen, 2021), though work is needed to verify their applicability to the tomography problem and optimize them for this
application.

745 While global optimization methods are comprehensive, they are also much more computationally expensive than the local
optimization method employed here with AT3D. Minimizing the amount of time spent in global optimization through the
improvement of the local optimization is always beneficial. Correspondingly, developing more effective initialization
strategies and other acceleration methods will improve the retrieval problem. Methods to estimate the order of magnitude of
750 the optical properties within the cloud have been proposed based on either a grid search of a low-dimensional cloud model
(Tzabari et al., 2022) or analytic radiative transfer results for idealized cloud geometries (Davis et al., 2021). Both of these
methods require cloud envelope information as input and stereo methods have shown promise at providing the required
information (Dandini et al., 2022). **Other methods to retrieve the internal extinction field are also possible such as using 1D
radiative transfer or heuristics based on 1D radiative transfer and linear tomography (Alexandrov et al., 2021). Both such**

755 methods neglect the asymmetry in the radiance field between forward and backward scattering geometries, which will lead to overestimation of the extinction field on the illuminated side of the cloud. An initialization with such an artefact would likely encourage the formation of the local minimum observed here in optically thick clouds with a gradient in extinction from the illuminated to shadowed side. Further study is needed to identify the most effective initialization methods and their range of applicability in terms of solar zenith angle and cloud optical depth.

760

We showed that the use of a low accuracy forward model has been demonstrated to provide potential in accelerating retrievals. However, when angular accuracy is reduced, the retrieval problem is sufficiently non-linear that the retrievals may diverge much further than expected due to forward model error alone. This means that a low accuracy forward model is not simply a tool to get to the same vicinity of state space quicker, at least when radiance measurements are the only constraint. While its use is beneficial for the naïve initialization used here, the benefit of using a low accuracy forward model must be tested in combination with other initialization methods to determine whether it has general utility. Our results show that the choice of angular resolution of the forward model and phase function is an important potential source of diversity in retrieval accuracy. This parameter should be considered carefully in future studies of tomography, especially when comparing performance between studies which have used a wide variety of model configurations (Levis et al., 2015; Martin and Hasekamp, 2018; Levis et al., 2020; Doicu et al., 2022a, b).

In general, the ill-conditioning of the forward model in the optically thick limit indicates that radiance measurements alone are not sufficient to constrain the retrieval problem. There are many potential sources of prior information that could be incorporated into the tomographic retrieval, particularly in the optically thick limit. These may be from LES, simpler models or statistics from other measurements such as in-situ cloud probes. The important consideration when incorporating prior data is to make sure that the resulting retrieval is used to test a hypothesis for which the prior is not relevant. For this reason, input from the wider cloud and aerosol physics communities will be invaluable in guiding the development of prior constraints for physics-based inversions or training data for statistical methods in the optically thick limit. The inclusion of other measurements such as cloud radar may also be instrumental in overcoming the limitations of the technique in optically thick clouds.

One of the main motivations for developing retrievals that use 3D radiative transfer is the need to reduce the systematic biases in the retrievals that vary with the solar and viewing geometry (Marshak et al., 2006; Kato and Marshak, 2009; Di Girolamo et al., 2010; Liang and Girolamo, 2013) and the instrument resolution (Marshak et al., 2006; Zhang et al., 2012). However, our analysis identified that systematic biases can exist in the optically thick limit that are aligned with the solar direction, despite the use of 3D radiative transfer. We hypothesize that no such biases will exist for scattering regimes similar to the Thin and Medium cloud categories examined here. Testing this hypothesis and quantifying the systematic variation of the biases

with solar and viewing geometry and instrument resolution is an important future step in the development and validation of the retrieval.

790 **6 Summary**

In this study, we have evaluated an algorithm for retrieving the 3D volumetric properties of clouds using multi-angle/multi-pixel radiances and 3D RT. The retrieval utilizes an iterative, optimization-based solution to the generalized least-squares problem to find a best-fitting state vector parameterizing the cloud's structure. The retrieval, which was described in detail in Part 1, is publicly available in the software AT3D.

795

We evaluated the tomographic retrieval by applying it to synthetic measurements with a known ground truth. The synthetic measurements were generated from 10 stochastically generated, cumuliform clouds in $(1 \text{ km})^3$ domains. The extinction fields of each cloud were scaled to have maximum optical depths of 4, 17.5, 44 and 88. The 3D fields of volume extinction coefficient are retrieved at 40 m resolution, a similar resolution to the radiance measurements (35 m).

800

When the target clouds have maximum optical depths less than 17 the relative RMSEs and relative biases of our idealized retrievals are less than 20% and 1%, respectively. Remaining errors in these clouds are limited to the small-scale ($< 250 \text{ m}$) spatial structure of the extinction field. The relative RMSEs in the retrieved extinction field grow with the optical depth of the cloud to reach an ensemble average of $\sim 70\%$ as the maximum optical thickness of the clouds reaches 88 (the value of our Very Thick cloud category). Errors become present at larger and larger spatial scales as the optical size of the cloud increases, including a notable decrease in retrieved extinction from the illuminated to the shadowed side of the cloud and with increasing optical distance from the sensors in the optically thick clouds. This particular error pattern is attributed to the ill-posedness of the retrieval in the optically thick limit and our choice of an optically thin initialization and use of a local optimization method to solve the inverse problem.

810

The retrievals of clouds in the optically thick limit are highly uncertain. The addition of radiometric noise can cause large deviations in the mean extinction of individual retrievals that reach 18% for these thick clouds, although ensemble-averaged retrieval behaviour remains unchanged. The choice of angular resolution in the forward model systematically modifies the behaviour of the retrieval result for the optically thickest clouds. Using a forward model with low angular accuracy that is **better-conditioned less ill-conditioned** results in the reduction of ensemble-averaged relative bias in the retrievals from -36% to just -8%, which exceeds the bias improvement from forward modelling error alone ($\sim 10\%$). This highlights the importance of the angular accuracy in SHDOM for setting the numerical stability of the inverse problem. We suggest that using forward models with low angular accuracy is an avenue for improving the fidelity and computational efficiency of retrievals.

815

820 The tomographic retrieval's inference of optical depth outperforms an IPA-based retrieval of optical depth. The IPA retrieval, which uses nadir radiance here, has biases worse than -23%. The tomographic retrieval's biases are much smaller for the clouds with optical depths less than 44 but are comparable for the thicker clouds unless the low angular accuracy forward model is used. Relative RMSEs for the optical depth are at worst half those of the IPA.

825 Overall, the proposed tomographic retrieval algorithm equipped with the approximate Jacobian calculation is most promising for shallow cumulus cloud fields over near-black surfaces (e.g. ocean). These clouds have the richest available information content within their multi-angle reflectances due to their highly heterogeneous nature. Therefore, from a fundamental perspective, these clouds are actually the easiest for passive tomographic remote sensing (Loveridge et al. 2022). Other optically thin clouds and aerosols are also likely to be effectively retrieved by this algorithm, which is an area for future work.

830

Deployment of the tomographic retrieval on the upcoming Cloud-CT mission (Schilling et al., 2019) has the potential to provide robust statistics of small-scale cloud properties unobtainable using in-situ measurements that are highly suitable for constraining model behaviour in climatically important shallow cumulus cloud fields. Further development of the retrieval is required to fully realize its potential of jointly retrieving aerosol and cloud properties and to improve its performance in more difficult, optically thicker or stratiform cloud regimes. Future work will improve the realism of the retrieval to develop a full uncertainty model for the retrieval for evaluation against real observations.

835

Appendix A

The noise model used for the measurements uses the specifications from NASA's Request for Information for a Tandem Stereo instrument related to the upcoming Atmospheric Observing System mission (NASA, 2021). The Tandem Stereo instrument would use narrowband cameras viewing in the visible at high spatial resolutions of around 50 m Ground Instantaneous Field of View per pixel. The Signal-to-Noise Ratio (SNR) requirement for this camera provides a reasonable proxy for the SNR that is achievable by an instrument that might be utilized for tomographic retrievals in practice. The SNR is defined as the ratio of the radiance, L , to the standard deviation of the radiance due to noise, σ_L . The SNR requirement for the Tandem Stereo camera is tabulated (Table A1) as a function of the equivalent reflectance, R , which is defined in terms of the band-averaged solar irradiance, F_0 , and the cosine of the solar zenith angle, μ_0

845

$$R = \frac{\pi L}{\mu_0 F_0}. \quad (\text{A1})$$

Table A1: The Signal-to-Noise Ratio (SNR) values tabulated as a function of equivalent reflectance used to generate noise for the measurements for the tomographic retrievals. See the text for details.

Equivalent Reflectance	0.01	0.05	0.1	0.5	1.0	1.3
SNR	87	201	285	639	904	1031

850 The SNR model for these measurements utilizes a cubic spline to interpolate between the values. No extrapolation at the upper end of the signal range is required. To extrapolate to reflectance values below the minimum we make the conservative assumption that the standard deviation of the radiance noise remains fixed below this reflectance level, which results in a linear decrease in the SNR till it reaches zero for no signal. This assumption is equivalent to assuming that the noise becomes dominated by dark noise below the minimum tabulated reflectance level.

855

The information provided is sufficient for an idealized modelling of the radiometric noise without modelling the details of the camera. We use a Poisson model to generate noise according to the SNR curve as both the photon and dark noise are well-modelled by this stochastic process and noise is typically limited by photon shot noise for most of the signal range. We neglect detailed models of other processes such as quantization, which are implicitly included in the required noise level.

860 The single parameter of the Poisson model, its rate, is uniquely defined as the square of the SNR. The number of counts produced in each realization of the Poisson process, N_L , is scaled back to a radiance by

$$L_{noisy} = \sqrt{N_L} \sigma_L^2.$$

Appendix B

The space carving algorithm implemented in AT3D performs a volume masking on a 3D property grid using the 2-D cloud masks as well as the geometric information associated with each pixel. Note that the geometric information requires not just the pixel information but also how each pixel's FOV is modelled, i.e., the geometry and weights of any sub-pixel rays. See Part 1 for how this is modelled in AT3D. The algorithm then proceeds simply by tracing each ray along its line-of-sight and counting the intersections of the ray with each grid-point in the volume of the domain. An intersection with a grid-point occurs whenever a ray intersects a grid-cell for which the grid-point is one of the bounding points. The intersections of clear and cloudy rays with each grid points are counted separately. A grid-point is designated as cloudy by a given image if the proportion of cloudy rays intersecting it for each mono-angle image is above a specified fraction (we use 0.0 for a clear conservative mask (Yang and Di Girolamo, 2008)). If the proportion of grid-point designations by each image is greater or equal to another specified fraction (typically 1.0), then the grid point is classified as cloudy. The threshold of 1.0 ensures that all grid points are designated as cloudy unless one view indicates that the grid point is clear. As such, the volume masking is clear conservative.

875

The accuracy of a space-carving algorithm of this sort is limited in multi-angle systems by angular resolution and spatial resolution (Lee et al., 2018). It is also limited by only using binary features (i.e., the cloud masks) to retrieve structural information and therefore can only retrieve detailed information on the cloud volume when the binary cloud masks are highly structured. Other stereoscopic approaches utilizing radiance feature matching (Seiz and Davies, 2006; Veikherman et al., 2015; 880 Bal et al., 2018) might perform better, especially in the case of stratiform clouds. However, in the case of cumuliform clouds, the performance of space-carving is quite good, especially at high spatial resolution, where the clear-conservative nature of the masking doesn't vastly overestimate cloud volumes.

When applied to the synthetic measurements used in the inversions, the true positive rate for grid-point classification across 885 all clouds is 10%, the true negative rate is 65%, the false positive rate is 25% and the false negative rate is 0%; so the true clouds take up only $\sim 10\%$ of the domain volume while the space carving algorithm estimates that they take up $\sim 35\%$.

Appendix C

In addition to the general setup of the inversion, we must make some specific choices about the optimization algorithm. The L-BFGS-B method is sensitive to the scaling of the problem in the initial iterations as the initial Hessian approximation in the 890 SciPy (Virtanen et al., 2020) implementation is simply the identity matrix. The first update to the state vector is therefore simply the gradient and is therefore sensitive to the size of the initial residuals. We choose the error-covariance matrix to be a diagonal matrix with entries of $10^{-8}/m$ to compensate this effect, where m is the number of measurements. With the solar flux chosen as unity (which sets the sizes of the radiances and residuals), this ensures that an initial step with a length of $\left\| \left. \frac{\partial \chi^2}{\partial \mathbf{a}} \right|_{\mathbf{a}_0} \right\|$ is not too small or too large in the sense that the Wolfe-Armijo conditions. The Wolfe-Armijo conditions on the line 895 search use the widely-used default parameter values of $c_1 = 0.9$ and $c_2 = 10^{-4}$ (Byrd et al., 1995; Zhu et al., 1997).

The L-BFGS-B method has two key hyper-parameters. The first is the number of past iterations of state and gradient changes used to approximate the Hessian of the cost function. This is chosen to be 10 iterations. The second is the maximum number of points to search in the line search during each iteration, which is also set to 10. Three stopping conditions are also specified, 900 the maximum number of iterations is 100, the minimum allowable relative change in the cost function before termination is set to 10^{-8} and the smallest maximum absolute value of the gradient before termination is also 10^{-8} . The maximum number of iterations for the "Restarted" retrievals is still 100, in addition to the 20 to 100 iterations at low angular accuracy used to form the initialization.

Code Availability

- 905 The software described and used in this paper is called Atmospheric Tomography with 3D Radiative Transfer (AT3D). A static archive of the software is available at Loveridge et al. (2022a). The most recent version is available from <https://github.com/CloudTomography/AT3D>. The original SHDOM code by Frank Evans is available from <https://nit.coloradolinux.com/~evans/shdom.html>.

Competing Interests

- 910 The authors declare that they have no conflict of interest.

Author Contributions

JL performed the investigation and prepared the initial draft under the supervision of LD. JL, LD, YS, AD, and AL conceptualized the study. JL, AL, VH and LF developed the software. All authors contributed to the editing of the manuscript.

Acknowledgments

- 915 The authors would like to thank Frank Evans for making his SHDOM code publicly available.
- Jesse Loveridge was supported by NASA's FINESST program under grant agreement 80NSSC20K1633. Aviad Levis is partially supported by the Zuckerman and Viterbi postdoctoral fellowships. This research was partially carried out at the Jet Propulsion Laboratory, California Institute of Technology, under a contract with the National Aeronautics and Space Administration (80NM0018D0004). Anthony Davis was supported by the ROSES NRA Program Element TASNPP17-0165.
- 920 Support from the MISR project through the Jet Propulsion Laboratory of the California Institute of Technology under Contract 1474871 for Larry Di Girolamo is gratefully acknowledged. Linda Forster was funded by the European Union's Framework Programme for Research and Innovation Horizon 2020 (2014–20) under the Marie Skłodowska-Curie Grant Agreement 754388 (LMUResearchFellows) and from LMUexcellent, funded by the Federal Ministry of Education and Research (BMBF) and the Free State of Bavaria under the Excellence Strategy of the German Federal Government and the
- 925 Länder. Yoav Schechner is the Mark and Diane Seiden Chair in Science at the Technion. He is a Landau Fellow - supported by the Taub Foundation. His work was conducted in the Ollendorff Minerva Center. Minerva is funded through the BMBF. This project has received funding from the European Union's Horizon 2020 research and innovation programme under grant agreement No 810370-ERC-CloudCT. The authors are grateful to the US-Israel Binational Science Foundation (BSF grant 2016325) for facilitating our international collaboration.

930 References

Abdoulaev, G. S., Ren, K., and Hielscher, A. H.: Optical tomography as a PDE-constrained optimization problem, *Inverse Problems*, 21, 1507–1530, <https://doi.org/10.1088/0266-5611/21/5/002>, 2005.

- Ahn, E., Huang, Y., Siems, S. T., and Manton, M. J.: A Comparison of Cloud Microphysical Properties Derived From MODIS and CALIPSO With In Situ Measurements Over the Wintertime Southern Ocean, *Journal of Geophysical Research: Atmospheres*, 123, 11,120–11,140, <https://doi.org/10.1029/2018JD028535>, 2018.
- Alexandrov, M. D., Emde, C., Van Diedenhoven, B., and Cairns, B.: Application of Radon Transform to Multi-Angle Measurements Made by the Research Scanning Polarimeter: A New Approach to Cloud Tomography. Part I: Theory and Tests on Simulated Data, *Frontiers in Remote Sensing*, 2, 2021.
- Arridge, S. R. and Schotland, J. C.: Optical tomography: forward and inverse problems, *Inverse Problems*, 25, 123010, <https://doi.org/10.1088/0266-5611/25/12/123010>, 2009.
- Bal, G.: Introduction to inverse problems, <https://statistics.uchicago.edu/~guillaumbal/PAPERS/IntroductionInverseProblems.pdf>, 2012.
- Bal, G. and Jollivet, A.: Stability estimates in stationary inverse transport, *Inverse Problems & Imaging*, 2, 427, <https://doi.org/10.3934/ipi.2008.2.427>, 2008.
- 945 Bal, G., Chen, J., and Davis, A. B.: Reconstruction of cloud geometry from high-resolution multi-angle images, *Inverse Problems & Imaging*, 12, 261, <https://doi.org/10.3934/ipi.2018011>, 2018.
- Bellouin, N., Quaas, J., Gryspeerdt, E., Kinne, S., Stier, P., Watson-Parris, D., Boucher, O., Carslaw, K. S., Christensen, M., Daniau, A.-L., Dufresne, J.-L., Feingold, G., Fiedler, S., Forster, P., Gettelman, A., Haywood, J. M., Lohmann, U., Malavelle, F., Mauritsen, T., McCoy, D. T., Myhre, G., Mülmenstädt, J., Neubauer, D., Possner, A., Rugenstein, M., Sato, Y., Schulz, M., Schwartz, S. E., Sourdeval, O., Storelvmo, T., Toll, V., Winker, D., and Stevens, B.: Bounding Global Aerosol Radiative Forcing of Climate Change, *Reviews of Geophysics*, 58, e2019RG000660, <https://doi.org/10.1029/2019RG000660>, 2020.
- Bitterli, B., Ravichandran, S., Müller, T., Wrenninge, M., Novák, J., Marschner, S., and Jarosz, W.: A radiative transfer framework for non-exponential media, *Computer Science Technical Reports*, 2018.
- Bruegge, C. J., Chrien, N. L., Ando, R. R., Diner, D. J., Abdou, W. A., Helmlinger, M. C., Pilorz, S. H., and Thome, K. J.: Early validation of the Multi-angle Imaging SpectroRadiometer (MISR) radiometric scale, *IEEE Transactions on Geoscience and Remote Sensing*, 40, 1477–1492, <https://doi.org/10.1109/TGRS.2002.801583>, 2002.
- 955 Byrd, R. H., Lu, P., Nocedal, J., and Zhu, C.: A Limited Memory Algorithm for Bound Constrained Optimization, *SIAM J. Sci. Comput.*, 16, 1190–1208, <https://doi.org/10.1137/0916069>, 1995.
- Cahalan, R. F., Ridgway, W., Wiscombe, W. J., Bell, T. L., and Snider, J. B.: The Albedo of Fractal Stratocumulus Clouds, *Journal of the Atmospheric Sciences*, 51, 2434–2455, [https://doi.org/10.1175/1520-0469\(1994\)051<2434:TAOFSC>2.0.CO;2](https://doi.org/10.1175/1520-0469(1994)051<2434:TAOFSC>2.0.CO;2), 1994.
- 960 Cahalan, R. F., Oreopoulos, L., Marshak, A., Evans, K. F., Davis, A. B., Pincus, R., Yetzer, K. H., Mayer, B., Davies, R., Ackerman, T. P., Barker, H. W., Clothiaux, E. E., Ellingson, R. G., Garay, M. J., Kassianov, E., Kinne, S., Macke, A., O’hirok, W., Partain, P. T., Prigarin, S. M., Rublev, A. N., Stephens, G. L., Szczap, F., Takara, E. E., Várnai, T., Wen, G., and Zhuravleva, T. B.: THE I3RC: Bringing Together the Most Advanced Radiative Transfer Tools for Cloudy Atmospheres, *Bulletin of the American Meteorological Society*, 86, 1275–1294, <https://doi.org/10.1175/BAMS-86-9-1275>, 2005.
- 965 Cairns, B., Lacis, A. A., and Carlson, B. E.: Absorption within Inhomogeneous Clouds and Its Parameterization in General Circulation Models, *Journal of the Atmospheric Sciences*, 57, 700–714, [https://doi.org/10.1175/1520-0469\(2000\)057<0700:AWICAI>2.0.CO;2](https://doi.org/10.1175/1520-0469(2000)057<0700:AWICAI>2.0.CO;2), 2000.

- 970 Chazette, P., Totems, J., Baron, A., Flamant, C., and Bony, S.: Trade-wind clouds and aerosols characterized by airborne horizontal lidar measurements during the EUREC⁴A field campaign, *Earth System Science Data*, 12, 2919–2936, <https://doi.org/10.5194/essd-12-2919-2020>, 2020.
- Chen, K., Li, Q., and Wang, L.: Stability of stationary inverse transport equation in diffusion scaling, *Inverse Problems*, 34, 025004, <https://doi.org/10.1088/1361-6420/aa990c>, 2018.
- 975 Dandini, P., Cornet, C., Binet, R., Fenouil, L., Holodovsky, V., Schechner, Y., Ricard, D., and Rosenfeld, D.: 3D cloud envelope and cloud development velocity from simulated CLOUD/C3IEL stereo images, *Atmospheric Measurement Techniques Discussions*, 1–37, <https://doi.org/10.5194/amt-2022-61>, 2022.
- Davis, A., Marshak, A., Wiscombe, W., and Cahalan, R.: Scale Invariance of Liquid Water Distributions in Marine Stratocumulus. Part I: Spectral Properties and Stationarity Issues, *Journal of the Atmospheric Sciences*, 53, 1538–1558, [https://doi.org/10.1175/1520-0469\(1996\)053<1538:SIOLWD>2.0.CO;2](https://doi.org/10.1175/1520-0469(1996)053<1538:SIOLWD>2.0.CO;2), 1996.
- 980 Davis, A., Marshak, A., Cahalan, R., and Wiscombe, W.: The Landsat Scale Break in Stratocumulus as a Three-Dimensional Radiative Transfer Effect: Implications for Cloud Remote Sensing, *Journal of the Atmospheric Sciences*, 54, 241–260, [https://doi.org/10.1175/1520-0469\(1997\)054<0241:TLSBIS>2.0.CO;2](https://doi.org/10.1175/1520-0469(1997)054<0241:TLSBIS>2.0.CO;2), 1997.
- Davis, A. B. and Marshak, A.: Photon propagation in heterogeneous optical media with spatial correlations: enhanced mean-free-paths and wider-than-exponential free-path distributions, *Journal of Quantitative Spectroscopy and Radiative Transfer*, 84, 3–34, [https://doi.org/10.1016/S0022-4073\(03\)00114-6](https://doi.org/10.1016/S0022-4073(03)00114-6), 2004.
- 985 Davis, A. B., Marshak, A., Gerber, H., and Wiscombe, W. J.: Horizontal structure of marine boundary layer clouds from centimeter to kilometer scales, *Journal of Geophysical Research: Atmospheres*, 104, 6123–6144, <https://doi.org/10.1029/1998JD200078>, 1999.
- 990 Davis, A. B., Forster, L., Diner, D. J., and Mayer, B.: Toward Cloud Tomography from Space using MISR and MODIS: The Physics of Image Formation for Opaque Convective Clouds, *arXiv:2011.14537 [physics]*, 2021.
- De Sterck, H. and Howse, A. J. M.: Nonlinearly preconditioned L-BFGS as an acceleration mechanism for alternating least squares with application to tensor decomposition, *Numerical Linear Algebra with Applications*, 25, e2202, <https://doi.org/10.1002/nla.2202>, 2018.
- 995 Delanoë, J. and Hogan, R. J.: A variational scheme for retrieving ice cloud properties from combined radar, lidar, and infrared radiometer, *Journal of Geophysical Research: Atmospheres*, 113, <https://doi.org/10.1029/2007JD009000>, 2008.
- Di Girolamo, L., Liang, L., and Platnick, S.: A global view of one-dimensional solar radiative transfer through oceanic water clouds, *Geophysical Research Letters*, 37, <https://doi.org/10.1029/2010GL044094>, 2010.
- Diner, D. J., Xu, F., Garay, M. J., Martonchik, J. V., Rheingans, B. E., Geier, S., Davis, A., Hancock, B. R., Jovanovic, V. M., Bull, M. A., Capraro, K., Chipman, R. A., and McClain, S. C.: The Airborne Multiangle SpectroPolarimetric Imager (AirMSPI): a new tool for aerosol and cloud remote sensing, *Atmospheric Measurement Techniques*, 6, 2007–2025, <https://doi.org/10.5194/amt-6-2007-2013>, 2013.
- 1000 Doicu, A. and Efremenko, D. S.: Linearizations of the Spherical Harmonic Discrete Ordinate Method (SHDOM), *Atmosphere*, 10, 292, <https://doi.org/10.3390/atmos10060292>, 2019.

- 1005 Doicu, A., Doicu, A., Efremenko, D., and Trautmann, T.: Cloud tomographic retrieval algorithms. I: Surrogate minimization method, *Journal of Quantitative Spectroscopy and Radiative Transfer*, 277, 107954, <https://doi.org/10.1016/j.jqsrt.2021.107954>, 2022a.
- Doicu, A., Doicu, A., Efremenko, D., and Trautmann, T.: Cloud tomographic retrieval algorithms. II: Adjoint method., *Journal of Quantitative Spectroscopy and Radiative Transfer*, 108177, <https://doi.org/10.1016/j.jqsrt.2022.108177>, 2022b.
- 1010 Dubovik, O., Herman, M., Holdak, A., Lapyonok, T., Tanré, D., Deuzé, J. L., Ducos, F., Sinyuk, A., and Lopatin, A.: Statistically optimized inversion algorithm for enhanced retrieval of aerosol properties from spectral multi-angle polarimetric satellite observations, *Atmospheric Measurement Techniques*, 4, 975–1018, <https://doi.org/10.5194/amt-4-975-2011>, 2011.
- Evans, K. F.: The Spherical Harmonics Discrete Ordinate Method for Three-Dimensional Atmospheric Radiative Transfer, *Journal of the Atmospheric Sciences*, 55, 429–446, [https://doi.org/10.1175/1520-0469\(1998\)055<0429:TSHDOM>2.0.CO;2](https://doi.org/10.1175/1520-0469(1998)055<0429:TSHDOM>2.0.CO;2),
1015 1998.
- Ewald, F., Zinner, T., Kölling, T., and Mayer, B.: Remote sensing of cloud droplet radius profiles using solar reflectance from cloud sides – Part 1: Retrieval development and characterization, *Atmospheric Measurement Techniques*, 12, 1183–1206, <https://doi.org/10.5194/amt-12-1183-2019>, 2019.
- 1020 Ewald, F., Groß, S., Wirth, M., Delanoë, J., Fox, S., and Mayer, B.: Why we need radar, lidar, and solar radiance observations to constrain ice cloud microphysics, *Atmospheric Measurement Techniques*, 14, 5029–5047, <https://doi.org/10.5194/amt-14-5029-2021>, 2021.
- Eytan, E., Khain, A., Pinsky, M., Altaratz, O., Shpund, J., and Koren, I.: Shallow Cumulus Properties as Captured by Adiabatic Fraction in High-Resolution LES Simulations, *Journal of the Atmospheric Sciences*, 79, 409–428, <https://doi.org/10.1175/JAS-D-21-0201.1>, 2022.
- 1025 Fielding, M. D., Chiu, J. C., Hogan, R. J., and Feingold, G.: A novel ensemble method for retrieving properties of warm cloud in 3-D using ground-based scanning radar and zenith radiances, *Journal of Geophysical Research: Atmospheres*, 119, 10,912–10,930, <https://doi.org/10.1002/2014JD021742>, 2014.
- Forster, L., Davis, A. B., Diner, D. J., and Mayer, B.: Toward Cloud Tomography from Space Using MISR and MODIS: Locating the “Veiled Core” in Opaque Convective Clouds, *Journal of the Atmospheric Sciences*, 78, 155–166, <https://doi.org/10.1175/JAS-D-19-0262.1>, 2021.
- 1030 Fu, D., Di Girolamo, L., Liang, L., and Zhao, G.: Regional Biases in MODIS Marine Liquid Water Cloud Drop Effective Radius Deduced Through Fusion With MISR, *Journal of Geophysical Research: Atmospheres*, 124, 13182–13196, <https://doi.org/10.1029/2019JD031063>, 2019.
- Fu, D., Di Girolamo, L., Rauber, R. M., McFarquhar, G. M., Nesbitt, S. W., Loveridge, J., Hong, Y., van Dierenhoven, B., Cairns, B., Alexandrov, M. D., Lawson, P., Woods, S., Tanelli, S., Schmidt, S., Hostetler, C., and Scarino, A. J.: An evaluation of the liquid cloud droplet effective radius derived from MODIS, airborne remote sensing, and in situ measurements from CAMP²Ex, *Atmospheric Chemistry and Physics*, 22, 8259–8285, <https://doi.org/10.5194/acp-22-8259-2022>, 2022.
- 1035 Gao, M., Franz, B. A., Knobelspiesse, K., Zhai, P.-W., Martins, V., Burton, S., Cairns, B., Ferrare, R., Gales, J., Hasekamp, O., Hu, Y., Ibrahim, A., McBride, B., Puthukkudy, A., Werdell, P. J., and Xu, X.: Efficient multi-angle polarimetric inversion of aerosols and ocean color powered by a deep neural network forward model, *Atmospheric Measurement Techniques*, 14, 4083–4110, <https://doi.org/10.5194/amt-14-4083-2021>, 2021.
- 1040

- Gao, M., Knobelspiesse, K., Franz, B. A., Zhai, P.-W., Sayer, A. M., Ibrahim, A., Cairns, B., Hasekamp, O., Hu, Y., Martins, V., Werdell, P. J., and Xu, X.: Effective uncertainty quantification for multi-angle polarimetric aerosol remote sensing over ocean, *Atmospheric Measurement Techniques*, 15, 4859–4879, <https://doi.org/10.5194/amt-15-4859-2022>, 2022.
- 1045 Guillaume, A., Kahn, B. H., Yue, Q., Fetzer, E. J., Wong, S., Manipon, G. J., Hua, H., and Wilson, B. D.: Horizontal and Vertical Scaling of Cloud Geometry Inferred from CloudSat Data, *Journal of the Atmospheric Sciences*, 75, 2187–2197, <https://doi.org/10.1175/JAS-D-17-0111.1>, 2018.
- Hu, C.-C. and van Leeuwen, P. J.: A particle flow filter for high-dimensional system applications, *Quarterly Journal of the Royal Meteorological Society*, 147, 2352–2374, <https://doi.org/10.1002/qj.4028>, 2021.
- 1050 Iwabuchi, H. and Hayasaka, T.: Effects of Cloud Horizontal Inhomogeneity on the Optical Thickness Retrieved from Moderate-Resolution Satellite Data, *Journal of the Atmospheric Sciences*, 59, 2227–2242, [https://doi.org/10.1175/1520-0469\(2002\)059<2227:EOCHIO>2.0.CO;2](https://doi.org/10.1175/1520-0469(2002)059<2227:EOCHIO>2.0.CO;2), 2002.
- Kato, S. and Marshak, A.: Solar zenith and viewing geometry-dependent errors in satellite retrieved cloud optical thickness: Marine stratocumulus case, *Journal of Geophysical Research: Atmospheres*, 114, <https://doi.org/10.1029/2008JD010579>, 2009.
- 1055 King, N. J. and Vaughan, G.: Using passive remote sensing to retrieve the vertical variation of cloud droplet size in marine stratocumulus: An assessment of information content and the potential for improved retrievals from hyperspectral measurements, *Journal of Geophysical Research: Atmospheres*, 117, <https://doi.org/10.1029/2012JD017896>, 2012.
- Kobayashi, T.: Parameterization of Reflectivity for Broken Cloud Fields, *Journal of the Atmospheric Sciences*, 45, 3034–3045, [https://doi.org/10.1175/1520-0469\(1988\)045<3034:PORFBC>2.0.CO;2](https://doi.org/10.1175/1520-0469(1988)045<3034:PORFBC>2.0.CO;2), 1988.
- 1060 Kutulakos, K. N. and Seitz, S. M.: A theory of shape by space carving, in: *Proceedings of the Seventh IEEE International Conference on Computer Vision, Proceedings of the Seventh IEEE International Conference on Computer Vision*, 307–314 vol.1, <https://doi.org/10.1109/ICCV.1999.791235>, 1999.
- Lebsock, M. and Su, H.: Application of active spaceborne remote sensing for understanding biases between passive cloud water path retrievals, *Journal of Geophysical Research: Atmospheres*, 119, 8962–8979, <https://doi.org/10.1002/2014JD021568>, 2014.
- 1065 Lee, B., Di Girolamo, L., Zhao, G., and Zhan, Y.: Three-Dimensional Cloud Volume Reconstruction from the Multi-angle Imaging SpectroRadiometer, *Remote Sensing*, 10, 1858, <https://doi.org/10.3390/rs10111858>, 2018.
- van Leeuwen, P. J., Künsch, H. R., Nerger, L., Potthast, R., and Reich, S.: Particle filters for high-dimensional geoscience applications: A review, *Quarterly Journal of the Royal Meteorological Society*, 145, 2335–2365, <https://doi.org/10.1002/qj.3551>, 2019.
- 1070 Levis, A., Schechner, Y. Y., Aides, A., and Davis, A. B.: Airborne Three-Dimensional Cloud Tomography, in: *2015 IEEE International Conference on Computer Vision (ICCV), 2015 IEEE International Conference on Computer Vision (ICCV)*, 3379–3387, <https://doi.org/10.1109/ICCV.2015.386>, 2015.
- Levis, A., Schechner, Y. Y., and Davis, A. B.: Multiple-Scattering Microphysics Tomography, in: *2017 IEEE Conference on Computer Vision and Pattern Recognition (CVPR), 2017 IEEE Conference on Computer Vision and Pattern Recognition (CVPR)*, 5797–5806, <https://doi.org/10.1109/CVPR.2017.614>, 2017.
- 1075

- Levis, A., Schechner, Y. Y., Davis, A. B., and Lloveridge, J.: Multi-View Polarimetric Scattering Cloud Tomography and Retrieval of Droplet Size, *Remote Sensing*, 12, 2831, <https://doi.org/10.3390/rs12172831>, 2020.
- 1080 Lewis, G. M., Austin, P. H., and Szczodrak, M.: Spatial statistics of marine boundary layer clouds, *Journal of Geophysical Research: Atmospheres*, 109, <https://doi.org/10.1029/2003JD003742>, 2004.
- Liang, L. and Girolamo, L. D.: A global analysis on the view-angle dependence of plane-parallel oceanic liquid water cloud optical thickness using data synergy from MISR and MODIS, *Journal of Geophysical Research: Atmospheres*, 118, 2389–2403, <https://doi.org/10.1029/2012JD018201>, 2013.
- 1085 Lovejoy, S., Schertzer, D., Silas, P., Tessier, Y., and Lavallee, D.: The unified scaling model of the atmospheric dynamics and systematic analysis of scale invariance in cloud radiances., *Annales Geophysicae*, 11, 119–127, 1993.
- Lloveridge, J., Levis, A., Holodovsky, V., and Forster, L.: Atmospheric Tomography with 3D Radiative Transfer, Zenodo [software], <https://doi.org/10.5281/zenodo.7025718>, 2022a.
- 1090 Lloveridge, J., Levis, A., Di Girolamo, L., Holodovsky, V., Forster, L., Davis, A. B., and Schechner, Y. Y.: Retrieving 3D distributions of atmospheric particles using Atmospheric Tomography with 3D Radiative Transfer – Part 1: Model description and Jacobian calculation, *Atmospheric Measurement Techniques Discussions*, 1–79, <https://doi.org/10.5194/amt-2022-251>, 2022b.
- 1095 Lloveridge, J., Levis, A., Di Girolamo, L., Holodovsky, V., Forster, L., Davis, A. B., and Schechner, Y. Y.: Retrieving 3D distributions of atmospheric particles using Atmospheric Tomography with 3D Radiative Transfer – Part 1: Model description and Jacobian calculation, *Atmospheric Measurement Techniques*, 16, 1803–1847, <https://doi.org/10.5194/amt-16-1803-2023>, 2023.
- Marshak, A., Davis, A., Wiscombe, W., and Cahalan, R.: Radiative smoothing in fractal clouds, *Journal of Geophysical Research: Atmospheres*, 100, 26247–26261, <https://doi.org/10.1029/95JD02895>, 1995.
- 1100 Marshak, A., Davis, A., Wiscombe, W., and Cahalan, R.: Radiative effects of sub-mean free path liquid water variability observed in stratiform clouds, *Journal of Geophysical Research: Atmospheres*, 103, 19557–19567, <https://doi.org/10.1029/98JD01728>, 1998.
- Marshak, A., Platnick, S., Várnai, T., Wen, G., and Cahalan, R. F.: Impact of three-dimensional radiative effects on satellite retrievals of cloud droplet sizes, *Journal of Geophysical Research: Atmospheres*, 111, <https://doi.org/10.1029/2005JD006686>, 2006.
- 1105 Martin, W., Cairns, B., and Bal, G.: Adjoint methods for adjusting three-dimensional atmosphere and surface properties to fit multi-angle/multi-pixel polarimetric measurements, *Journal of Quantitative Spectroscopy and Radiative Transfer*, 144, 68–85, <https://doi.org/10.1016/j.jqsrt.2014.03.030>, 2014.
- Martin, W. G. K. and Hasekamp, O. P.: A demonstration of adjoint methods for multi-dimensional remote sensing of the atmosphere and surface, *Journal of Quantitative Spectroscopy and Radiative Transfer*, 204, 215–231, <https://doi.org/10.1016/j.jqsrt.2017.09.031>, 2018.
- 1110 Miller, D. J., Zhang, Z., Platnick, S., Ackerman, A. S., Werner, F., Cornet, C., and Knobelspiesse, K.: Comparisons of bispectral and polarimetric retrievals of marine boundary layer cloud microphysics: case studies using a LES–satellite retrieval simulator, *Atmospheric Measurement Techniques*, 11, 3689–3715, <https://doi.org/10.5194/amt-11-3689-2018>, 2018.

- 1115 Morrison, H., van Lier-Walqui, M., Fridlind, A. M., Grabowski, W. W., Harrington, J. Y., Hoose, C., Korolev, A., Kumjian, M. R., Milbrandt, J. A., Pawlowska, H., Posselt, D. J., Prat, O. P., Reimel, K. J., Shima, S.-I., van Diedenhoven, B., and Xue, L.: Confronting the Challenge of Modeling Cloud and Precipitation Microphysics, *Journal of Advances in Modeling Earth Systems*, 12, e2019MS001689, <https://doi.org/10.1029/2019MS001689>, 2020.
- 1120 Nakajima, T. and Tanaka, M.: Algorithms for radiative intensity calculations in moderately thick atmospheres using a truncation approximation, *Journal of Quantitative Spectroscopy and Radiative Transfer*, 40, 51–69, [https://doi.org/10.1016/0022-4073\(88\)90031-3](https://doi.org/10.1016/0022-4073(88)90031-3), 1988.
- NASA: AtmOS Tandem Stereographic Cameras Instrumentation, https://aos.gsfc.nasa.gov/docs/ATMOS_Tandem_Stereographic_Cameras_210602+final+revised.pdf, 8 June 2021.
- 1125 Nataraja, V., Schmidt, S., Chen, H., Yamaguchi, T., Kazil, J., Feingold, G., Wolf, K., and Iwabuchi, H.: Segmentation-based multi-pixel cloud optical thickness retrieval using a convolutional neural network, *Atmospheric Measurement Techniques*, 15, 5181–5205, <https://doi.org/10.5194/amt-15-5181-2022>, 2022.
- Niu, H., Lin, Z.-J., Tian, F., Dhamne, S., and Liu, H.: Comprehensive investigation of three-dimensional diffuse optical tomography with depth compensation algorithm, *J Biomed Opt*, 15, 046005, <https://doi.org/10.1117/1.3462986>, 2010.
- 1130 Painemal, D., Spangenberg, D., Smith Jr., W. L., Minnis, P., Cairns, B., Moore, R. H., Crosbie, E., Robinson, C., Thornhill, K. L., Winstead, E. L., and Ziemba, L.: Evaluation of satellite retrievals of liquid clouds from the GOES-13 imager and MODIS over the midlatitude North Atlantic during the NAAMES campaign, *Atmospheric Measurement Techniques*, 14, 6633–6646, <https://doi.org/10.5194/amt-14-6633-2021>, 2021.
- Peherstorfer, B., Willcox, K., and Gunzburger, M.: Survey of Multifidelity Methods in Uncertainty Propagation, Inference, and Optimization, *SIAM Rev.*, 60, 550–591, <https://doi.org/10.1137/16M1082469>, 2018.
- 1135 Pincus, R. and Evans, K. F.: Computational Cost and Accuracy in Calculating Three-Dimensional Radiative Transfer: Results for New Implementations of Monte Carlo and SHDOM, *Journal of the Atmospheric Sciences*, 66, 3131–3146, <https://doi.org/10.1175/2009JAS3137.1>, 2009.
- Prigarin, S. M. and Marshak, A.: A Simple Stochastic Model for Generating Broken Cloud Optical Depth and Cloud-Top Height Fields, *Journal of the Atmospheric Sciences*, 66, 92–104, <https://doi.org/10.1175/2008JAS2699.1>, 2009.
- 1140 Raveendran, T., Gupta, S., Vasu, R. M., and Roy, D.: Pseudo-time particle filtering for diffuse optical tomography, *J. Opt. Soc. Am. A*, JOSAA, 28, 2070–2081, <https://doi.org/10.1364/JOSAA.28.002070>, 2011.
- Rodgers, C. D.: *Inverse Methods for Atmospheric Sounding*, WORLD SCIENTIFIC, <https://doi.org/10.1142/3171>, 2000.
- Ronen, R., Holodovsky, V., and Schechner, Y. Y.: Variable Imaging Projection Cloud Scattering Tomography, *IEEE Transactions on Pattern Analysis and Machine Intelligence*, 1–12, <https://doi.org/10.1109/TPAMI.2022.3195920>, 2022.
- 1145 Schilling, K., Schechner, Y. Y., and Koren, I.: CloudCT - Computed Tomography Of Clouds By A Small Satellite Formation, 12th IAA symposium on Small Satellites for Earth Observation, 2019.
- Schmetz, J.: On the parameterization of the radiative properties of broken clouds, *Tellus A: Dynamic Meteorology and Oceanography*, 36, 417–432, <https://doi.org/10.3402/tellusa.v36i5.11644>, 1984.
- Seiz, G. and Davies, R.: Reconstruction of cloud geometry from multi-view satellite images, *Remote Sensing of Environment*, 100, 143–149, <https://doi.org/10.1016/j.rse.2005.09.016>, 2006.

- 1150 Sherwood, S. C., Bony, S., and Dufresne, J.-L.: Spread in model climate sensitivity traced to atmospheric convective mixing, *Nature*, 505, 37–42, <https://doi.org/10.1038/nature12829>, 2014.
- Sherwood, S. C., Webb, M. J., Annan, J. D., Armour, K. C., Forster, P. M., Hargreaves, J. C., Hegerl, G., Klein, S. A., Marvel, K. D., Rohling, E. J., Watanabe, M., Andrews, T., Braconnot, P., Bretherton, C. S., Foster, G. L., Hausfather, Z., von der Heydt, A. S., Knutti, R., Mauritsen, T., Norris, J. R., Proistosescu, C., Rugenstein, M., Schmidt, G. A., Tokarska, K. B., and Zelinka, M. D.: An Assessment of Earth’s Climate Sensitivity Using Multiple Lines of Evidence, *Reviews of Geophysics*, 58, e2019RG000678, <https://doi.org/10.1029/2019RG000678>, 2020.
- 1155 Shi, H.-J. M., Xie, Y., Byrd, R., and Nocedal, J.: A Noise-Tolerant Quasi-Newton Algorithm for Unconstrained Optimization, *arXiv:2010.04352 [math]*, 2021.
- Tarvainen, T., Kolehmainen, V., Pulkkinen, A., Vauhkonen, M., Schweiger, M., Arridge, S. R., and Kaipio, J. P.: An approximation error approach for compensating for modelling errors between the radiative transfer equation and the diffusion approximation in diffuse optical tomography, *Inverse Problems*, 26, 015005, <https://doi.org/10.1088/0266-5611/26/1/015005>, 2009.
- 1160 Tian, F., Niu, H., Khadka, S., Lin, Z.-J., and Liu, H.: Algorithmic depth compensation improves quantification and noise suppression in functional diffuse optical tomography, *Biomed. Opt. Express*, BOE, 1, 441–452, <https://doi.org/10.1364/BOE.1.000441>, 2010.
- 1165 Tzabari, M., Holodovsky, V., Shubi, O., Eytan, E., Koren, I., and Schechner, Y. Y.: Settings for Spaceborne 3-D Scattering Tomography of Liquid-Phase Clouds by the CloudCT Mission, *IEEE Transactions on Geoscience and Remote Sensing*, 60, 1–16, <https://doi.org/10.1109/TGRS.2022.3198525>, 2022.
- Veikherman, D., Aides, A., Schechner, Y. Y., and Levis, A.: Clouds in the Cloud, in: *Computer Vision -- ACCV 2014*, Cham, 659–674, https://doi.org/10.1007/978-3-319-16817-3_43, 2015.
- 1170 Virtanen, P., Gommers, R., Oliphant, T. E., Haberland, M., Reddy, T., Cournapeau, D., Burovski, E., Peterson, P., Weckesser, W., Bright, J., van der Walt, S. J., Brett, M., Wilson, J., Millman, K. J., Mayorov, N., Nelson, A. R. J., Jones, E., Kern, R., Larson, E., Carey, C. J., Polat, İ., Feng, Y., Moore, E. W., VanderPlas, J., Laxalde, D., Perktold, J., Cimrman, R., Henriksen, I., Quintero, E. A., Harris, C. R., Archibald, A. M., Ribeiro, A. H., Pedregosa, F., and van Mulbregt, P.: SciPy 1.0: fundamental algorithms for scientific computing in Python, *Nat Methods*, 17, 261–272, <https://doi.org/10.1038/s41592-019-0686-2>, 2020.
- 1175 Weinman, J. A. and Harshvardhan: Solar reflection from a regular array of horizontally finite clouds, *Appl. Opt.*, AO, 21, 2940–2944, <https://doi.org/10.1364/AO.21.002940>, 1982.
- Wiscombe, W. J.: The Delta–M Method: Rapid Yet Accurate Radiative Flux Calculations for Strongly Asymmetric Phase Functions, *Journal of the Atmospheric Sciences*, 34, 1408–1422, [https://doi.org/10.1175/1520-0469\(1977\)034<1408:TDMRYA>2.0.CO;2](https://doi.org/10.1175/1520-0469(1977)034<1408:TDMRYA>2.0.CO;2), 1977.
- 1180 Xu, Z., Mace, G. G., and Posselt, D. J.: Impact of Rain on Retrieved Warm Cloud Properties Using Visible and Near-Infrared Reflectances Using Markov Chain Monte Carlo Techniques, *IEEE Transactions on Geoscience and Remote Sensing*, 60, 1–10, <https://doi.org/10.1109/TGRS.2022.3208007>, 2022.
- 1185 Yang, Y. and Di Girolamo, L.: Impacts of 3-D radiative effects on satellite cloud detection and their consequences on cloud fraction and aerosol optical depth retrievals, *Journal of Geophysical Research: Atmospheres*, 113, <https://doi.org/10.1029/2007JD009095>, 2008.

- Zhang, Z., Ackerman, A. S., Feingold, G., Platnick, S., Pincus, R., and Xue, H.: Effects of cloud horizontal inhomogeneity and drizzle on remote sensing of cloud droplet effective radius: Case studies based on large-eddy simulations, *Journal of Geophysical Research: Atmospheres*, 117, <https://doi.org/10.1029/2012JD017655>, 2012.
- 1190 Zhao, G. and Di Girolamo, L.: Statistics on the macrophysical properties of trade wind cumuli over the tropical western Atlantic, *Journal of Geophysical Research: Atmospheres*, 112, <https://doi.org/10.1029/2006JD007371>, 2007.
- Zhao, H. and Zhong, Y.: Instability of an Inverse Problem for the Stationary Radiative Transport Near the Diffusion Limit, *SIAM J. Math. Anal.*, 51, 3750–3768, <https://doi.org/10.1137/18M1222582>, 2019.
- 1195 Zhu, C., Byrd, R. H., Lu, P., and Nocedal, J.: Algorithm 778: L-BFGS-B: Fortran subroutines for large-scale bound-constrained optimization, *ACM Trans. Math. Softw.*, 23, 550–560, <https://doi.org/10.1145/279232.279236>, 1997.